5-8-2015

Discrimination of Problem Seismic Events by Modeling the Combined Effects of Deterministic and Statistical Structure on Regional Seismograms

Michele Fitzpatrick
University of Connecticut - Storrs, mfitz@tvcconnect.net

Discrimination of Problem Seismic Events by Modeling the Combined Effects of Deterministic and Statistical Structure on Regional Seismograms

Michele Fitzpatrick, Ph.D.

University of Connecticut, 2015

Monitoring the Comprehensive Nuclear Test Ban Treaty requires analysts to discriminate seismic signals generated by earthquakes vs nuclear explosions. Seismologists are generally able to discriminate large energy events (> 5 mb) at teleseismic distances (greater than about 1,000 km). However, lower energy events need to be analyzed at regional distances because the energy attenuates with distance. At regional distances (< 1,000 km), the seismic energy travels primarily through the Earth's crust and can be affected by large- and small-scale crustal structures. This can have the effect of making earthquakes look more like explosions and vice versa and is very dependent on the region through which the energy travels. Therefore new methods are needed to assist in the discrimination of events recorded at regional distances.

The work discussed here uses a new computer code to model the combined effects of known 3-D relatively large (deterministic) Earth structures and relatively small (statistical) structures to generate improved structural models and evaluate the performance of yield estimators and discriminants at selected seismic stations in Eurasia. This is accomplished by synthesizing seismograms using a radiative transport technique to predict the high frequency coda (>2-5 Hz) of regional seismic phases at stations having known relatively large, three-dimensional structure, combined with experiments to estimate the effects of multiple-scattering from unknown smaller structures.

Discrimination of Problem Seismic Events by Modeling the Combined Effects of Deterministic and Statistical Structure on Regional Seismograms

Michele Fitzpatrick

B.S., U.S. Coast Guard Academy, 1980

M.S., Naval Postgraduate School, 1986

A Dissertation

Submitted in Partial Fulfillment of the

Requirements for the Degree of

Doctor of Philosophy

at the

University of Connecticut

2015

APPROVAL PAGE

Doctor of Philosophy Dissertation

Discrimination of Problem Seismic Events by Modeling the Combined Effects of Deterministic and Statistical Structure on Regional Seismograms

Presented by

Michele Fitzpatrick, B.S., M.S.

Major Advisor _____

Dr. Vernon Cormier

Associate Advisor _____

Dr. Lanbo Liu

Associate Advisor _____

Dr. Timothy B. Byrne

University of Connecticut
2015

ACKNOWLEDGEMENTS

I would like to thank the members of the UCONN Solid Earth Geophysics Research Group, without whose assistance this work would not have been possible. My sincerest thanks go to Dr. Vernon Cormier, my Primary Advisor. Christopher Sanborn is primarily responsible for the development of Radiative3D, and I truly appreciate his efforts, our valuable discussions, and his responsiveness in producing Radiative3D results. Steven Walsh helped with code modifications and production of some of the code results used in this study. Nil Mistry was an undergraduate student who helped with the early Earth model work.

This research was funded by AFRL/DOE Contract No. FA9453-12-C-0207, May 30, 2012 through May 29, 2015.

TABLE OF CONTENTS

LIST OF TABLES

LIST OF FIGURES

LIST OF ACRONYMS

2-D	Two-dimensional
3-D	Three-dimensional
ACF	Auto correlation function
AFTAC	Air Force Technical Applications Center
CMT	Centroid Moment Tensor
CTBT	Comprehensive Nuclear Test Ban Treaty
CTBTO	Comprehensive Nuclear-Test-Ban Treaty Organization
DOE	Department of Energy
Hz	Hertz
IDC	International Data Center
IMS	International Monitoring System
IRIS	Incorporated Research Institutions for Seismology
km	Kilometer
kt	Kiloton
LTBT	Limited Test Ban Treaty
mb	Body wave magnitude
MFP	Mean-free-path
Ms	Surface wave magnitude
Mw	Moment magnitude
NEIC	National Earthquake Information Center
NRC	National Research Council
NTM	National Technical Means
OSI	On-site Inspection
PDE	Preliminary Determination of Epicenters
PSDF	Power Spectral Density Function
REB	Reviewed Event Bulletin
RUM	Regionalized upper mantle
SEB	Standard Event Bulletin
SEL	Standard Event List
SSEB	Standard Screened Event Bulletin
USGS	U.S. Geological Survey

CHAPTER 1

Monitoring the Comprehensive Nuclear Test Ban Treaty

1.1 INTRODUCTION

The Comprehensive Nuclear Test Ban Treaty (CTBT), opened for signature in 1996, prohibits nuclear test explosions and any other nuclear explosions in all environments: underground, in the oceans, and in the atmosphere. Although the treaty is not yet ratified by all of the required nations, the Comprehensive Nuclear Test Ban Treaty Organization (CTBTO) established by the treaty performs the functions specified in the treaty. This includes operating an International Data Center (IDC) headquartered in Vienna, Austria, processing and reporting on data from an International Monitoring System (IMS), and receiving and processing requests for on-site inspections (OSIs) (Coyne et al., 2012). According to the treaty, only citizens of ratified signatories may serve as the Director-General, inspectors, or members of the professional and clerical staff (CTBTO, 1996).

The IDC receives and processes seismic data and provides list of events to the CTBT community. One of these lists, the Standard Screened Event Bulletin (SSEB), contains events which failed standard criteria for discrimination between earthquakes and explosions (Coyne et al., 2012). Under the CTBT the actual identification of problem or anomalous seismic events as either nuclear explosions or earthquakes is reserved for national CTBT authorities using National Technical Means (NTM). In the U.S., the Air Force Technical Applications Center (AFTAC) is the authority that applies additional analytical techniques to these events. AFTAC's NTM provides monitoring capability that is superior to that of the IMS and can focus on monitoring countries of concern to the United States (NRC, 2012). However, most of the NTM processes used by AFTAC are classified and unavailable to the public.

Seismologists are generally able to discriminate large energy events (> 5 mb) at teleseismic distances (greater than about 1,000 km). However, lower energy events need to be

analyzed at regional distances because the energy attenuates with distance. At regional distances (< 1,000 km), the seismic energy travels primarily through the Earth's crust and can be affected by large- and small-scale crustal structures. This can have the effect of making earthquakes look more like explosions and vice versa and is very dependent on the region through which the energy travels (e.g., Hartse et al., 1997). Therefore new methods are needed to assist in the discrimination of events recorded at regional distances (NRC, 1997).

The work discussed here uses a new computer code to model the combined effects of known three-dimensional (3-D) relatively large (deterministic) Earth structures and relatively small (statistical) structures to generate improved structural models and evaluate the performance of yield estimators and discriminants at selected seismic stations in Eurasia. This is accomplished by synthesizing seismograms using a radiative transport technique to predict the high frequency coda (>2-5 Hz) of regional seismic phases at stations having known relatively large, three-dimensional structures, combined with experiments to estimate the effects of multiple-scattering from unknown relatively small structures.

1.2 MONITORING THE CTBT

The IMS is comprised of monitoring facilities as specified in the CTBT. It consists of a global network of seismic sensors, ocean bottom hydrophone sensors, surface acoustic sensors, and surface and airborne radionuclide sensors. The work discussed in this document focuses on the type of data generated by seismic sensors. Primary seismic stations send continuous near-real-time data to the IDC. Auxiliary seismic stations provide data when requested by the IDC. Data from the IMS networks are automatically processed at the IDC. While signals from some sources can be discarded as noise, there is a wide range of sources which generate signals which

must be processed, analyzed, and reviewed. The location and time of these sources are subsequently reported by the IDC in its bulletins. Automatic bulletins are called the Standard Event Lists (SEL1, SEL2, SEL3). After analyst review and correction as necessary the Reviewed Event Bulletin (REB) is produced (Coyne et al., 2012).

Interactive analysis is performed by analysts to review and correct results of SEL3 data and to add missed events and discard invalid events. After analyst review, the Reviewed Event Bulletin (REB) is produced. The Standard Event Bulletin (SEB) is produced automatically shortly after the REB, and it includes additional information about characterization of an event as an earthquake or otherwise. The Standard Screened Event Bulletin (SSEB) contains events which failed standard criteria for discrimination. The ISC bulletin is freely available from the CTBTO website (Coyne et al., 2012).

The process of monitoring the CTBT involves systematic screening of all types of signals detected by the monitoring network for the purpose of identifying those from any nuclear explosion that might take place (NRC, 2012). The research discussed in this document concentrates on technical means of seismic detection, separate from the other means (hydroacoustic and radionuclide). The challenge lies in distinguishing signals generated by natural or benign human-induced sources from those of a nuclear explosion against a background of ambient noise.

1.2.1 Stages for Seismic Detection

At every stage of the monitoring operation there are basic functions that must be performed that depend on the scientific understanding of the phenomena. Stages for seismic detection include:

- Event detection and association
- Source location
- Size estimation
- Source interpretation or discrimination
- Attribution

This section includes a short discussion of each of these stages based on NRC (1997) and NRC (2012). The remainder of the dissertation will focus on discrimination.

1.2.1.1 Event Detection and Association

The first substantial signal processing step in CTBT monitoring is the detection of signals of the type that could be emitted by a nuclear explosion. This involves continuously searching seismic (and other) signals for changes in the background "noise" level or the appearance of spatially correlated energy with little or no change in signal level or spectra. Each underground event creates a variety of signals due to near-source effects and the heterogeneity of the Earth's elastic structure along the paths of seismic waves detected at the network stations. The pattern of signals varies from station to station, and the signals from the many nonnuclear sources overlap and mask each other. Once signals are detected they are grouped together to be associated with a specific event.

1.2.1.2 Source Location

An event location is defined by the latitude, longitude, depth, and time at which the energy release occurred. The association process generates an approximate location for an event, which must then be refined. The estimate of the source location is obtained by minimizing the

difference between the observed and predicted arrival times of seismic waves at the network stations. The predicted times are from a model of the Earth's elastic structure.

The arrival times of regional waves depend strongly on the extremely heterogeneous, shallow crustal structure. Seismologists usually take "regional" to mean within 1,000 km or less from the earthquake or explosion. Longer range observations are called teleseismic. Earth models often have a uniform crustal layer, and the deviations between the actual and calculated arrival times for regional waves are often larger than those found for teleseismic observations. As a result, it is difficult to locate an event based only on regional arrival times or small numbers of teleseismic and regional arrivals.

Source location will be particularly important in cases where CTBTO authorities or member parties wish to conduct OSIs. Part II of the Treaty's Protocol says that the area of an on-site inspection shall be continuous and its size shall not exceed 1,000 square km. There shall be no linear distance greater than 50 km in any direction (CTBTO, 1996). Therefore the starting location for an OSI needs to be accurate to about 10 km.

1.2.1.3 *Size Estimation*

Monitoring operations need to interpret the strength of seismic signals in terms of the physical energy released at the source. This includes defining the explosion yield levels associated with diverse monitoring thresholds, as well as being part of event identification procedures. Seismologists usually measure yield in mass of equivalent chemical explosion. It is related to energy release and empirically calibrated against seismic magnitude. Various technologies make different contributions to estimating size.

If an event is identified confidently as a nuclear explosion, it is then possible to estimate the yield of the explosion from empirical or theoretical knowledge of how explosion sources

generate the observed signals. Analysts must understand the propagation effects for seismic waves in order to relate observed signal amplitudes to source energy release, and this must be done without prior knowledge of the source type. In effect, there is a need to know the variation of signal amplitudes with distance from a source for different frequencies and wave types. This allows the effective source strength to be estimated as a function of frequency and signal type, which provides the basis for many event identification procedures.

Seismic event size or magnitude is based on measuring the amplitude of particular phases on seismograms (USGS, 2014). The four most common measures of magnitude are:

- mb – body wave magnitude, which is measured using short period (frequencies around 1 Hz) teleseismic P-waves
- Ms – surface wave magnitude, which is measured using 20-second period surface waves, which are dispersed waves traveling along the surface of the earth and exponentially decay with depth
- Mb (Lg) – peak amplitude of a group of high frequency (>1 Hz) S seismic waves trapped and guided in earth's crust (short-period surface waves at regional distances).
- Mw – moment magnitude, a modernization of the seismic magnitude related to earthquake faulting area and slip or explosion cavity volume, more accurately related the frequency dependence of the radiated energy than mb and Ms

1.2.1.4 *Source Interpretation or Discrimination*

For CTBT monitoring purposes, the source identification process primarily consists of determining which events are definitely *not* nuclear tests. For example, accurate determination that the depth of a source in a continental region is greater than 10 km ensures that it is not a

human-induced event. This is because the deepest borehole ever drilled (Kola Peninsula) was 10 km or less, and it is technically unfeasible to drill deeper due to geothermal lithostatic pressure gradients (Fuchs et al., 1990).

The extent to which the monitoring network can accurately determine critical location parameters, such as depth and location, greatly impacts the number of events that must be identified based on other signal characteristics. There will inevitably be many events that are not identified by straight-forward procedures. For these events, more information must be extracted from the signals. As with other monitoring functions, event identification capabilities will vary geographically and with the medium under consideration.

1.2.1.5 Attribution

If a nuclear test occurs, verification ultimately requires the ability to identify the nation or organization responsible for it. Various monitoring technologies may indicate a high probability that a nuclear device has been detonated at a particular location. This must be verified by on-site, near on-site, or possibly remote-site detection of fission products. Given that a nuclear explosion has been identified, attribution in the CTBT context can occur in three generic ways either alone or in combination: (1) national technical means (NTM) or intelligence assets identify the nation or organization associated with the explosion; (2) the identified explosion occurs at a location that can be demonstrated to be under the control of a particular nation or organization; and/or (3) analysis of the debris or artifacts from an identified event reveals characteristics that can be associated with a specific nation or organization.

1.2.2 Discrimination Process

The discrimination process requires an understanding of the differences between earthquake and explosion sources, and the effects those differences have on seismic recordings.

Seismologists currently use a number of methods to analyze events, which are discussed in this section. Some of these methods work well for high energy events. New and/or improved methods are needed for the low energy or yield events that are likely to occur in the future (NRC, 1997).

1.2.3 Earthquake and Explosion Sources

Potential sources in the bulletins include earthquakes, non-nuclear explosions, volcanoes, and meteorites. An underground nuclear explosion releases energy in microseconds. The energy of the explosion vaporizes the surrounding rock, producing a cavity filled with gas that can have pressures of several million atmospheres. This gas expands outward rapidly, sending a compressional shock wave into the surrounding rock. This shock wave initially melts and shatters the rock as it propagates. The rock will eventually respond elastically, returning to its initial state after the disturbance passes by. At this point, called the elastic radius, the wave becomes a compressional seismic wave (P wave). The explosion source process is rapid relative to natural earthquake events of comparable total energy release (NRC, 1997).

An ideal explosion source will radiate P-wave energy in a uniform, isotropic, spherical wavefront, although actual underground nuclear explosions are often more complex (Walter et al., 2007). Asymmetries in material properties around the source, as well as cracking and shearing of rock above the shotpoint, and relaxation of ambient tectonic stresses in the rock volume surrounding the explosion cavity can all generate a smaller fraction of S waves, which involves transient shear deformation of the medium (NRC, 1997). Both P and S waves are referred to as body waves because they travel through the Earth's interior.

Earthquake faulting typically involves shearing displacements across a fault surface, generating stronger S-wave radiation than P-wave radiation and longer surface waves. The

magnitude of the earthquake increases with fault length (Brune, 1970 and Richards and Zavales, 1990). Figure 1.1 schematically depicts source energy patterns for an idealized sub-surface explosion and a tectonic earthquake (of pure strike-slip type) in a homogeneous medium.

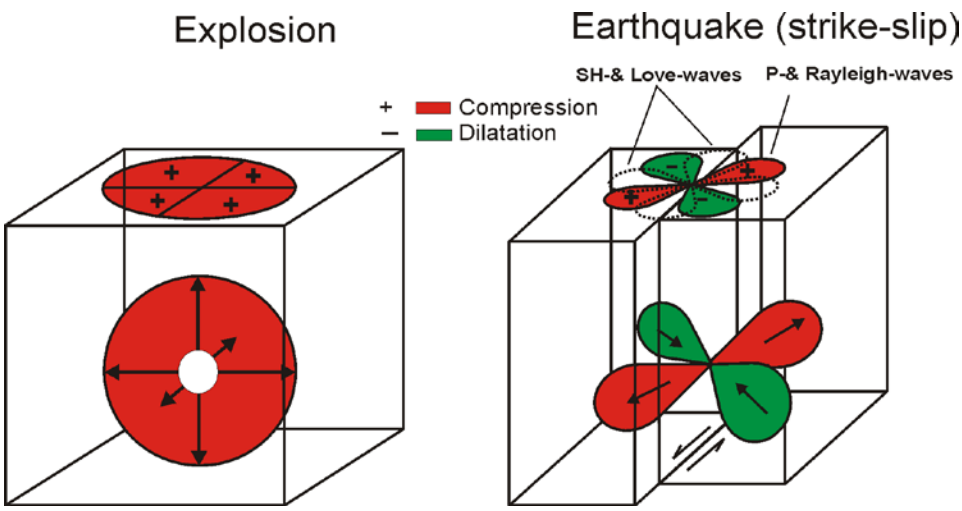

Figure 1.1. Schematic of idealized explosion and earthquake sources.
(from http://ebooks.gfz-potsdam.de/pubman/item/escidoc%3A4015/component /escidoc%3A4016/Chapter_3_rev1.pdf)

The physical dimension of the source volume of explosions is much smaller than the fault zone for a natural earthquake of comparable energy release. This difference decreases at small magnitudes, and attenuation may eliminate the frequencies at which the differences could be easily observed. For both explosions and earthquakes, only a small fraction of the total energy released at the source is contained in the elastic wavefield (NRC, 1997).

The rapid onset time scale and compact source dimensions of underground nuclear explosions directly affect the frequency spectrum of seismic wave energy radiated by the source. Explosions of comparable body-wave magnitude excite more high-frequency oscillations than earthquakes (Mueller and Murphy, 1971). Figure 1.2 shows "source spectra" of ground

displacement (left) and velocity (right) for a seismic shear source and a 1 kiloton (kt) underground nuclear explosion (Shearer and Almann, 2006).

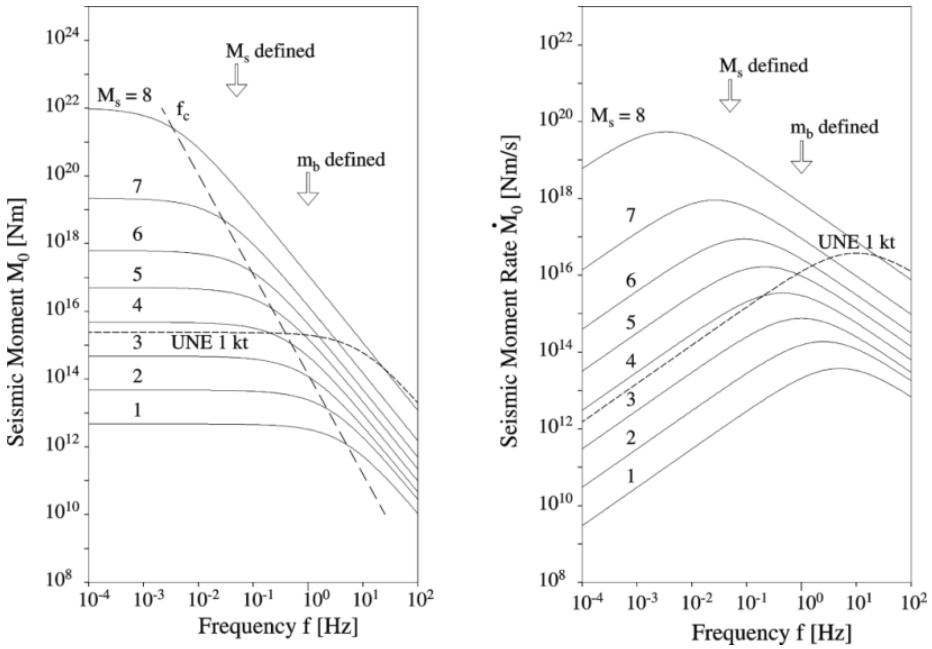

Figure 1.2. Source spectra of ground displacement (left) and velocity (right). (From Shearer and Almann, 2006)

These source spectra show that the differences between earthquakes and explosions are largest in the highest recordable frequency band (> 2 Hz). The scattering of seismic energy also increases at high frequencies. There are limited techniques for modeling high frequency seismograms in the sense of handling the effects of relatively small 3-D structures, which become important when wavelengths are on the order of the 1-100 km length scales of velocity and density fluctuations due to the lithologic heterogeneity concentrated in earth's crust and upper mantle. Accurate seismograms can be synthesized for these effects using numerical methods to integrate equations of motion in small scale 3-D structure, but are practically limited with current computational power to less than 100 to 200 wavelengths (Hestholm et al., 1994)

1.2.4 Methods Used for Discrimination

The depth of the source, the spatial extent of the source, the rate at which source energy is released, and the geometry of the source process all control the relative levels and frequency content of P and S energy released into the surrounding medium (and their partitioning into body and surface waves). Resulting variations in the properties of seismic waves generated by these sources lie at the heart of seismic discrimination methods. The methods generally used to discriminate seismic events include (NRC, 1997 and NRC, 2012):

- Values of mb-Ms
- Focal mechanisms (CMT-Centroid Moment Tensor)
- Well-determined depths
- Clear first motions
- Presence of foreshock/aftershock sequences
- Ratio of high-frequency P to Lg seismic waves at regional distances

Values of mb-Ms – This method looks at surface wave energy relative to the energy in the initial P-phase. These are measured in different frequency bands (1 Hz and 0.05 Hz), and hence can detect differences in the spectral shapes of radiated elastic energy. It does not provide an estimate of event depth. Ms as measured traditionally between periods of about 18 to 21 seconds is difficult to detect in the presence of noise for events smaller than about mb = 4.

Focal mechanisms (CMT-Centroid Moment Tensor) – utilizes broadband seismic body and surface waves to determine the focal mechanism of the event. CMTs can be obtained for moderate-size events. CMT solutions often utilize the period band 25 to 100 seconds where earth noise is low.

Well-determined depths – computed from the seismic depth phases pP and sP (Heyburn and Bowers, 2008). Explosion sources are located within the upper kilometer or so of the crust, whereas most earthquakes occur at greater depths. A depth significantly greater than about 3 km indicates that an event cannot be an underground nuclear explosion (Sykes and Nettles, 2009).

Clear first motions. The first motions of P waves from earthquakes with reverse-faulting mechanisms, as at Lop Nor, typically are compressional (upward) at stations at large (teleseismic) distances. In that case a seismic event cannot be discriminated as either an explosion or an earthquake. With the advent of data from short distances, however, clear dilatational (downward) first motion of P is sometimes observed. Such an observation indicates that the event cannot be an explosion.

Ratio of high-frequency Pn to Lg seismic waves at regional distances. The method uses the relative amplitudes of regional waves Pn (first to arrive) and Lg (most prominent high frequency phase) because they are usually the easiest to identify (Xie, 2002).

Comparison of the relative behavior of various measures of source strength tuned to different frequencies or wavetypes (e.g., mb and Ms), can distinguish the different types of sources in some cases. The empirical trends observed in such measures establish a basis for identifying a given source type, although these indirect measures must be viewed as statistical indicators (NRC, 1997).

For large events (mb > 4.5), the mb:Ms comparisons made for teleseismic measurements provide one of the most robust seismic discriminants between explosions and earthquakes. For CTBT monitoring, in which small events are of interest, application of the traditional form of this discriminant is limited by the fact that small events do not excite the necessary surface waves, independent of the type of source (Hartse et al., 1997).

In current practice, a suite of regionally calibrated discriminants must serve for small event (mb < 4) identification purposes, with sequential application of the discriminant or a statistical combination of the event identification probabilities provided by the various methods being used to define the confidence level for identification for the suite (NRC, 1997).

1.2.5 Discrimination Concerns

The year after the CTBT was released for signature, the National Research Council published a report discussing the monitoring implications for the United States and the research required to support the U.S. monitoring program. Seismologists are generally able to discriminate large energy events (> 5 mb) at teleseismic distances. However, lower energy events need to be analyzed at regional distances because the energy dissipates with distance. Hartse et al. (1997) noted there is a question about how effective the discriminants using magnitude ratios will be for explosions whose magnitudes fall below mb ~ 4.

1.2.6 Problem Events

The seismic events that are most interesting to national authorities are those that fail the standard criteria for discrimination between earthquakes and explosions. Sykes and Nettles (2009) report that about 70 events detected during the 50 years prior to their study were singled out in openly available scientific and governmental publications or the media as problem events whose identification potentially compromises the verifiability of the CTBT. These events are a tiny fraction of the earthquakes processed and reported by CTBT authorities. However, since many occurred either near nuclear test sites or in a few countries that may be seeking nuclear capabilities, they have been, and continue to be, of great importance to policy makers. Since earthquakes will continue to occur, their identification will continue to constitute a main task of insuring compliance with the CTBT (NRC, 2012).

1.3 REGIONAL SEISMIC PHASES

For decades following the Limited Test Ban Treaty (LTBT), when nuclear testing was carried out underground and in-country monitoring was not permitted, monitoring was conducted using teleseismic signals. These signals have relatively simple propagation effects that are now well understood. Using such data, global detection, location, and identification of all underground events above magnitude 4.5 appears to be straightforward given an adequate distribution of recording facilities (NRC, 2012).

Teleseismic signals are weak, however, for the small events of interest for CTBT monitoring (mb < 4, including events with magnitudes as low as 2.0 in some regions). Consequently, treaty verification will necessitate increased dependence on regional signals of these small events, observed at distances less than about 1,000 km (NRC, 2012). These signals are complicated by reverberations in the crust, but they often have good signal-to-noise ratios. Though regional waves can have large amplitudes (and thus be detected easily if a seismometer is operated at a regional distance from a source of interest), they are more complex and harder to interpret than teleseismic waves.

1.3.1 Regional Seismic Wave Definition

Regional waves primarily travel in the low-velocity crust (25 to 70 km thick in continental regions) and uppermost mantle, often interacting with the crust-mantle interface, known as the Moho. Seismic wave amplitudes at regional distances are strong near the source but decrease in amplitude with distance and can be too small to detect beyond 1,000 km. The term "regional" can carry the additional implication that such waves are dependent on the properties of the Earth's crust and uppermost mantle, which can vary quite strongly from one region to another (NRC, 2012). Figure 1.3 shows the general paths of some of the regional

phases. Table 1.1 lists the wave types and gives a typical velocity and arrival time for two regional distances.

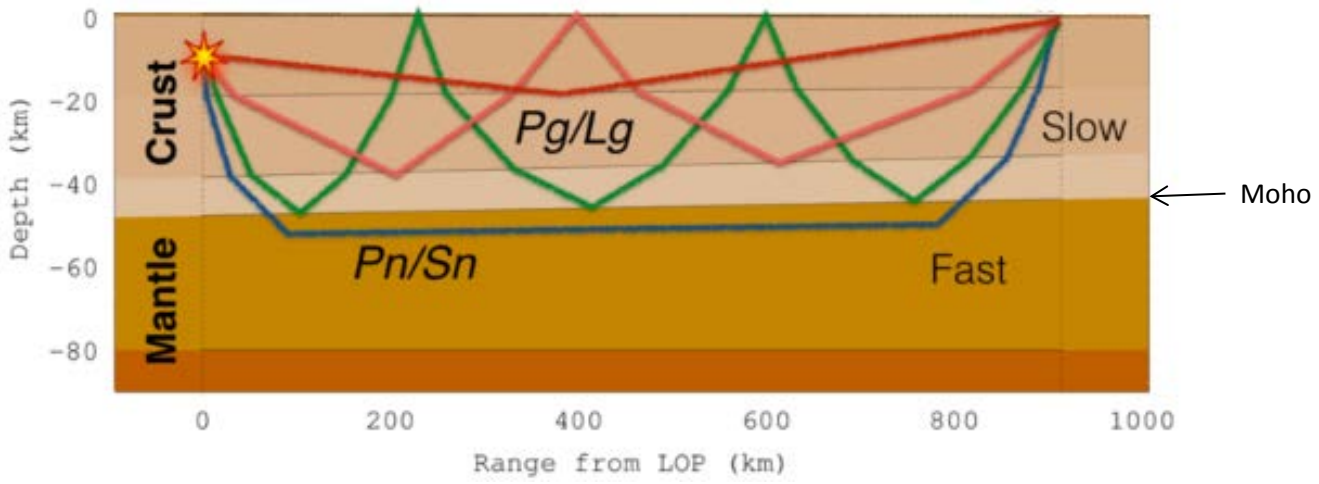

Figure 1.3. Regional seismic phases.

Table 1.1. Regional phase velocities.

Name	Phase Velocity (approximate)	Propagation	~ Arrival (800 km)	~ Arrival (1000 km)
Pn	8 km /sec	Moho P interference head wave	100 s	125 s
Pg	6 km/sec	Crustal body P wave(s)	133 s	167 s
Sn	4.6 km/sec	Moho S interference head wave	174 s	217 s
Lg	3.5 - 4 km/sec	Crustal body S wave(s)	200-228 s	250-286 s
Rg	3.1 km/sec	Fundamental mode Rayleigh	258 s	323 s

Phase velocity is the apparent velocity of a wavefront along the surface of the earth. For example, a wavefront parallel to the surface, corresponding to wavefront propagation in the vertical direction, has an infinite phase velocity, i.e., the wavefront arrives at all receivers simultaneously. Be measuring arrival times of waves arriving at receivers along the surface, it is possible to determine the angle of approach of the wavefront and hence its phase velocity. This can be done by stacking and time shifting records according to the time shift expected for the arrival of wavefronts having different phase velocities.

Pg and Lg are known as crustal phases because their energy is mostly contained in the crust. The Pg seismic phase consists of direct P-wave energy from crustal earthquakes or explosions and is usually found in a velocity window between 5.0 and 6.5 km. The Lg seismic phase consists of the superposition of multiple critically reflected S waves from the Moho and free surface (Storchak, 2003). They can usually be found within velocity and frequency windows of 3.1 to 3.6 km/sec and 0.5 to 5.0 Hz, respectively. The Lg phase can be the most important of the regional waves for purposes of explosion monitoring because it is typically the largest wave observed in a seismogram at a regional distance. These are the phases modeled by the original version of Radiative3D.

The first prominent phase on the seismic record for regional distances is Pn, a mantle lid guided wave with a velocity window of 7.8 to 8.1 km/sec. Pn can be a "head wave," but head waves in plane layered media are too small in amplitude to be Pn. It is now better understood as an "interference head wave" consisting of a P wave turning below the Moho, with a bunch of constructively inferring underside reflections from the Moho (Storchak, 2003).

The Sn phase is a high-frequency guided seismic wave that travels in the lithospheric mantle with a typical frequency of 1 to 4 Hz or more. The typical velocity for Sn is around 4.7 km/sec in stable continental and oceanic lithosphere and less than that in more tectonically active regions (Storchak, 2003).

Rg is a high frequency fundamental mode Rayleigh surface wave, which travels along surface and exponentially decays with depth. It is dispersive, with different frequencies traveling at different velocities (Storchak, 2003).

The minimum distance for arrivals of Pn and Lg, will be governed by crustal structure, but it will be the distance for which a downward propagating P or S wave incident on the Moho can excite a Moho reflected P or S wave at greater than the post critical reflection angle.

1.3.2 Discrimination Issues with Regional Phases

At regional distances (< 1,000 km), the seismic energy travels primarily through the Earth's crust and can be affected by large- and small-scale crustal structures. This will have the effect of making earthquakes look more like explosions and vice versa and is very dependent on the region through which the energy travels. Therefore new methods are needed to assist in the discrimination of events recorded at regional distances (NRC, 1997). Fisk (2006) noted that a lack of theoretical understanding of the P and S waves produces by earthquakes and explosions reduces the confidence in P/S ratios for operational modeling.

Some examples of how regional effects complicate discrimination include:

- The Lg phase can be important in discrimination because earthquakes should have more Lg energy than explosions (Hartse et al., 1997 and Baumgardt, 2001). However, observations of Lg propagation have demonstrated that the Lg wave may be blocked for paths in oceanic or very thin continental crust (Al-Damegh et al., 2004).
- There has been much discussion about why regional shear waves are excited by underground nuclear explosions given that the initial blast consists of only P waves (Toksoz and Kehrer, 1972; Hong and Xie, 2005; Walter et al., 2007; and references therein). If the Lg energy associated with an explosion is from a nonisotropic secondary source, the spectral character may be more similar to earthquakes (Hartse et al., 1997).

- Sub-crustal earthquakes (depths between approximately 50 and 300 km in typical continental crust) are known to sometimes have explosion-like characteristics, attributable to their impulsive, high-frequency P-waves and relatively weak high-frequency S-waves. Hartse et al. (1997) found that some sub-crustal earthquakes in the Lop Nor region of China Sub-crustal earthquakes were rich in short period P energy, deficient in Lg energy, and lacking the strong surface waves of other earthquakes from the same region.
- Pedersen et al. (1998) noted problems with the measurement of Ms due to surface wave conversions from changes in crustal thickness as seen in some Lop Nor explosion data at certain receivers in western Europe.

Al-Damegh et al. (2004) focused on understanding the propagation characteristics of the regional seismic waves Pn, Pg, Sn and Lg. In particular, Lg is shown to be sensitive to lateral variations in the crustal thickness as well as the rheology of the crustal rocks. Sn, however, is very sensitive to lateral variations in the mantle lid and/or to the presence of asthenospheric material very close or immediately below the crust.

1.4 LOP NOR REGION

We chose the Lop Nor region of China as our study area for a number of reasons:

- Publicly available nuclear explosion data through the Incorporated Research Institutions for Seismology (IRIS) web site.
- Recent earthquakes near the explosion site.
- “Problem” earthquake that occurred in 2003.

The Chinese nuclear test site known as Lop Nor is located near the southeastern side of the Tien Shan, a region of moderate earthquake activity and contemporary horizontal

compressive stress in the earth's crust (Matzko, 1994). Molnar and Tapponnier (1975) suggested most of the regional tectonics of Asia are a result of the India-Eurasia collision, which results in broad zones of deformation across China, in which China is being deformed and squeezed out to the east. Figure 1.4 shows the relative location of Lop Nor within China (~ 40 N, 90 E).

Figure 1.4. Map showing Lop Nor, China.
(from http://en.wikipedia.org/wiki/File:China_edcp_location_map.svg)

1.4.1 Lop Nor Geology

Lop Nor is located in the northeastern edge of the Tarim basin, an unusual geologic province. The Tarim basin is a rigid block of Precambrian and Paleozoic rocks which have survived relatively undeformed during the ongoing India-Eurasian collision. To the north of the Tarim basin is the Tien Shan; to the south is the Tibetan Plateau and the Hindu Kush. Most of the Tarim basin is covered with a Quaternary sedimentary sequence, although at the Lop Nor test

site the sedimentary cover is thin. The basement at the test site consists mainly of metaconglomerates, sandstones, and some Carboniferous-age granite. The basement outcrops as small knobs and ridges (Matzko, 1994). Recent information on the Moho depth in China can be found in He et al. (2014).

1.4.2 Explosion History

The Chinese underground nuclear test site in the Kuruktag and Kyzyltag mountains of the Xinjiang Uygur Autonomous Region of northwest China, is the location of at least twenty-one underground tests that occurred between 1969 and 1996 (see Table 1.2). The largest test, conducted on 21 May 1992, had a reported yield of about one megaton. Geophysical properties of the rocks and a regional geologic map of part of the test area were published by the Chinese in 1986 and 1987 and are the first site-specific data available for this test site. Figure 1.5 shows a representation of the layout (Gupta, 1995).

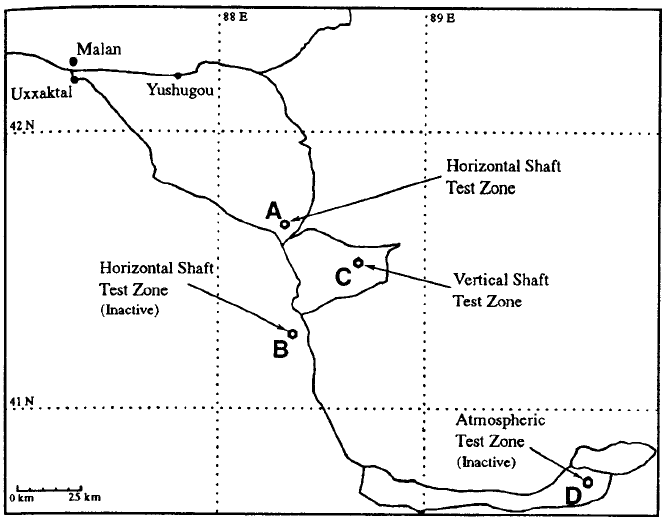

Figure 1.5. Layout of the underground nuclear test site at Lop Nor.
(from Gupta, 1995)

The events are clustered in two groups. The events in the western portion of the test site are thought to have been detonated in horizontal shafts. The events in the basin are vertical

emplacements (Wallace and Tinker, 1996). Waldhauser et al. (2004) provide additional details on the locations of the explosions.

Table 1.2. Lop Nor underground nuclear tests.

Date	Time	Lat (N)	Lon (E)	yield (kt)/ Mb
1969 SEPT 22		41.35	88.33	-/5.2
1975 OCT 27		41.43	88.40	-/5.0
1976 OCT 17		41.64	88.21	-/4.9
1978 OCT 14		41.42	88.66	-/4.9
1983 MAY 4		41.13	88.31	-/4.5
1983 OCT 6		41.53	88.72	-/5.5
1984 OCT 3		41.54	88.67	-/5.4
1984 DEC 19		41.62	88.22	-/4.7
1987 JUN 5		41.55	88.72	-/6.2
1988 SEPT 29		41.76	88.39	-/5.0
1990 MAY 26	7:59:58	41.56	88.68	15-65/5.4
1990 AUG 16	4:59:58	41.514	88.739	189/6.2
1992 MAY 21	4:59:58	41.513	88.774	660/6.5
1992 SEPT 25	7:59:58	41.716	88.336	1-2/5.4
1993 OCT 5	1:59:57	41.7	88.6	90/5.8
1994 JUN 10	6:25:58	41.64	88.86	90/5.8
1994 OCT 7	3:25:58	41.55	89.07	90/6.0
1995 MAY 15	4:05:58	41.63	88.87	95/6.1
1995 AUG 17	0:59:58	41.6	88.86	90/6.0
1996 JUN 8	2:55:58	41.65	88.76	50/5.9
1996 JUL 29	1:48:58	41.82	88.42	3/4.7

1.4.3 Earthquake History

There have been a number of major earthquakes in the Lop Nor region, including several within 20 km of the explosion site. For example, Sykes and Nettles (2009) found that more than half of the total numbers of earthquakes in the Reviewed Event Bulletin (REB) of the IMS that occurred within 100 km (62 mi) of six test sites from 2000 through 2008 occurred near Lop Nor. Table 1.3 gives the details for some of these events (http://ds.iris.edu/wilber3/find_event). Figure

1.6 shows the area we're currently investigating. Seismic stations MAK (46.808 N, 81.977 E) and WUS (41.199 N, 79.218 E) are approximately 8^{o} from Lop Nor.

Table 1.3. Selected Lop Nor area earthquake events.

Date	Time	LAT(N)	LON(E)	Depth	mb
1987 DEC 22	00:16:39	41.316	89.615	21	5.5 (Mw)
1988 SEP 29	07:00:01	41.524	88.154	33	4.7
1988 NOV 15	16:56:45	42.035	89.354	26	4.9
1990 NOV 3	17:25:14	40.847	89.031	22	5.1
1992 NOV 27	16:09:09	41.960	89.262	14.3	5.3
1995 MAR 18	18:02:36	42.400	87.172	21.8	5.2
1999 JAN 27	06:25:02	41.553	88.355	41.4	4.5
1999 JAN 30	03:51:05	41.586	88.455	21	5.4 (Mw)
2003 FEB 13	18:32:47	41.819	88.062	61.3	4.3
2003 MAR 13	15:07:06	41.656	88.987	32	4.8
2004 JUL 8	18:36:34	41.843	88.121	34.5	4.1
2005 OCT 11	14:48:15	41.752	87.576	33	4.1
2007 NOV 18	11:35:18	42.279	88.123	21	4.1
2009 NOV 11	01:17:16	41.968	88.136	44	4.4
2011 JUN 8	01:53:26	43.035	88.251	22.4	5.1 (Mw)
2012 JAN 8	06:26:31	42.137	87.307	15.8	4.9 (Mw)
2012 OCT 6	09:27:40	41.131	88.331	36	4.7

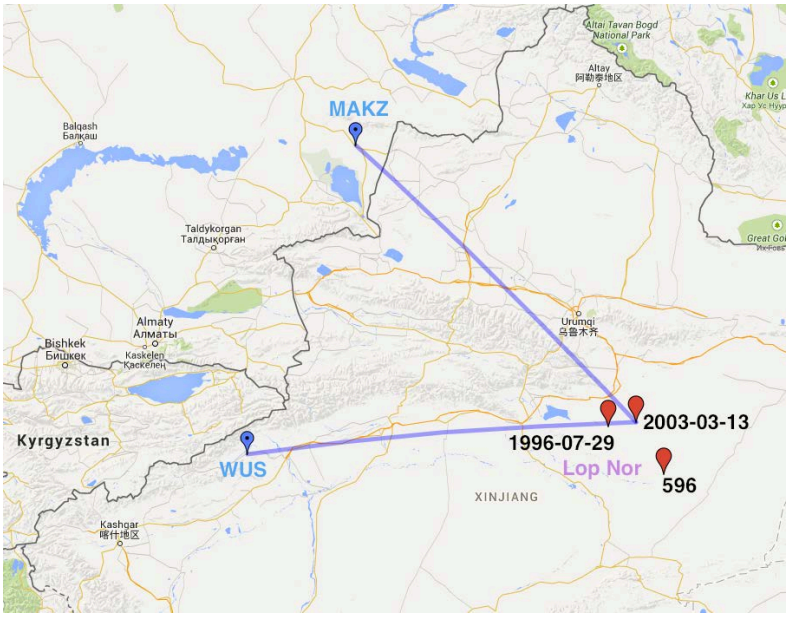

Figure 1.6. Relative location of Lop Nor explosions, earthquakes, and stations.

1.4.4 Problem Event

At about 1500 UTC on March 13, 2003 a seismic disturbance (subsequently referred to as 2003-03-13) occurred near the nuclear test site at Lop Nor. The National Earthquake Information Center (NEIC) of the U.S. Geological Survey (USGS) reported an origin time of 15:07:07, an epicenter of 41.797_ N, 89.079_ E, and a bodywave magnitude of mb = 4.8 in its Preliminary Determination of Epicenters (PDE) bulletin. The PDE reported a (fixed) depth of 33 km, and no surface waves (and consequently no Ms value) were associated with 2003-03-13 (Selby et al., 2005).

Because 2003-03-13 occurred close to the Lop Nor site, it was of immediate interest to those monitoring compliance with the Comprehensive Nuclear-Test-Ban Treaty (CTBT). As discussed earlier, the International Data Centre (IDC) is charged with producing a number of bulletins. Of particular interest here, the IDC is required under the terms of the CTBT to produce a "screened" bulletin, which lists seismic disturbances that cannot be confidently identified as earthquakes (note that the IDC is not required to positively identify events as explosions). Event 2003-03-13 was originally "unidentified" and required special study.

A number of groups studied the event and provided publicly available information about it. Selby et al. (2005) identified the event as an earthquake but with some equivocation. They combined three types of seismic data: (1) teleseismic P seismograms recorded at current IMS stations; (2) long-period surface waves recorded at stations across Eurasia which simulate the proposed IMS primary and auxiliary seismic network, and (3) waveform modeling of the three-component long-period seismogram recorded at station WMQ in northwest China. They concluded that the observations are consistent with a double-couple source with strike $\phi = 125 \pm 10^{o}$, dip $\delta = 40 \pm 10^{o}$, rake $\delta = 90 \pm 10^{o}$, moment $M_o = 5.5 \pm 1 \text{ X } 10^{15}$ N m, and an estimated

focal depth of 6 ± 1 km. Sykes and Nettles (2009) obtained a reliable CMT with a similar mechanism and depth, which they concluded clearly identified it as an earthquake.

This result reinforces the importance of focal depth determination to CTBT monitoring, in particular, for shallow earthquakes with mechanisms that are close to perfect 45^{o} reverse-dip-slip, which are difficult to discriminate by using other methods (Sykes and Nettles, 2009). The fact that this event required additional analysis to determine its source type makes it useful for further study.

1.5 REFERENCES

Al-Damegh, K., Sandvol, E., Al-Lazki, A., and Barazangi, M. (2004). Regional seismic wave propagation (Lg and Sn) and Pn attenuation in the Arabian plate and surrounding regions, Geophys. J. Int.., 157, 775-795.

Baumgardt, D.R. (2001). "Sedimentary basins and blockage of Lg wave propagation in continents", Pure and Appl. Geophys., 158, 2001, pp.1207-1250.

Brune, J.N. (1970). "Tectonic Stress and the Spectra of Seismic Shear Waves from Earthquakes", J. Geophys. Res., 75, 1970, pp. 4997-5009.

Coyne, John, Dmitry Bobrov, Peter Bormann (Germany), Emerenciana Duran, Patrick Grenard, Georgios Haralabus, Ivan Kitov, and Yuri Starovoit (2012). New Manual of Seismological Observatory Practice Chapter 17, CTBTO: Goals, Networks, Data Analysis and Data Availability (Version: January 2012; DOI: 10.2312/GFZ.NMSOP-2_ch17)

CTBTO (Comprehensive Test Ban Treaty Organization) (1996). Retrieved from http://www.ctbto.org/the-treaty/.

Fisk, M. D. (2006). Source spectral modeling of regional P/S discriminants at nuclear test sites in China and the Former Soviet Union, Bull. Seism. Soc. Am. 96: 2348–2367.

Fuchs, K., E.A. Kozlovsky, A.I. Krivtsov, and M.D. Zoback (Eds.) (1990). Super-Deep Continental Drilling and Deep Geophysical Sounding. Springer Verlag, Berlin, 436 p.

Gupta, Vipin (1995). Locating Nuclear Explosions at the Chinese Test Site near Lop Nor, *Science & Global Security, Volume 5*, pp. 205-244, 1995.

Hartse, H.E., S.R. Taylor, W.S. Phillips, and G.E. Randall (1997).A preliminary study of regional seismic discrimination in Central Asia with emphasis on Western China, Bulletin of the Seismological Society of America Vol 87. No. 3, pp. 551-568, June 1997.

He, R., X. Shang, C. Yu, H. Zhang, and R.D. Van der Hilst (2014). A unified map of Moho depth and Vp /Vs ratio of continental China by receiver function analysis, *Geophysical Journal International*, doi: 10.1093/gji/ggu365, 2014.

Hestholm, S. O., Husebye, E. S. and Ruud, B. O. (1994), Seismic wave propagation in complex crust-upper mantle media using 2-D finite-difference synthetics. *Geophysical Journal International*, 118: 643–670. doi: 10.1111/j.1365-246X.1994.tb03991.x

Heyburn, R., and D. Bowers (2008). Earthquake depth estimations using the F trace and associated probability, Bulletin of the Seismological Society of America 98: 18-35.

Hong, T.-K., and J. Xie (2005), Phase composition of regional seismic waves from underground nuclear explosions, *J. Geophys. Res*., 110, B12302, doi:10.1029/2005JB003753.

Matzko, J.R. (1994). Geology of the Chinese nuclear test site near Lop Nor, Xinjiang Uygur autonomous region, China, Engineering Geology, 36, 173-181.

Molnar, P. and P. Tapponnier (1975). "Cenozoic Tectonics of Asia: Effects of a Continental Collision," *Science* Volume 189, Number 4201, pp. 419-426, 8 August 1975.

Mueller, R.A., and J.R. Murphy (1971). "Seismic characteristics of underground nuclear detonations: Part I. Seismic spectrum scaling", *Bull. Seism. Soc. Am.*, **61**, 1971, pp. 1675-1692.

NRC (1997). National Research Council Panel on Basic Research Requirements in Support of Comprehensive Test Ban Monitoring. Research Required to Support Comprehensive Nuclear Test Ban Treaty Monitoring. National Academy Press, ISBN: 0-309-59079-5, 150 pages, (1997), http://www.nap.edu/catalog/5875.html

NRC (2012). National Research Council Committee on Reviewing and Updating Technical Issues Related to the Comprehensive Nuclear Test Ban Treaty; Policy and Global Affairs; The Comprehensive Nuclear Test Ban Treaty: Technical Issues for the United States, ISBN 978-0-309-14998-3, (2012), http://www.nap.edu/catalog.php?record_id=12849.

Pedersen, H.A., Avouac, J-P., and Campillo, M. (1998). "Anomalous surface waves from Lop Nor nuclear explosions: observations and numerial modeling", *J.Geophys. Res*., **103**, 1998, pp. 15,051-15,068.

Richards, P.G. and J. Zavales (1990). "Seismic Discrimination of Nuclear Explosions", Annu. Rev. Earth Planet. Sci. 1990, 18:257-86.

Selby, N.D., D. Bowers, A. Douglas, R. Heyburn, and D. Porter (2005). Seismic discrimination in southern Xinjiang: The 13 March 2003 Lop Nor earthquake. Bulletin of the Seismological Society of America 95(1):197-211.

Shearer, P.M. and B.P. Almann (2006). Spectral Studies of Shallow Earthquakes and Explosions in Southern California, 28th Seismic Research Review: Ground-Based Nuclear Explosion Monitoring Technologies, 2006.

Storchak, D.A., J. Schweitzer, and P. Bormann (2003), "The IASPEI Standard Seismic Phase List", Seismol. Res. Lett. 74, 6, 761-772.

Sykes, L.R., and M. Nettles (2009). Dealing with Hard-to-identify Seismic Events Globally and those near Nuclear Test Sites. Poster presented at the International Scientific Studies Conference. Comprehensive Nuclear Test Ban Treaty Organization, Vienna, Austria. Available at: http://www.ctbto.org/fileadmin/user_upload/ISS_2009/Poster/SEISMO-26J%20(US)%20-%20Lynn_Sykes%20and%20Meredith_Nettles.pdf.

Toksoz, M.N., and H.H. Kehrer (1972). Tectonic strain release by underground nuclear explosions and its effect on seismic discrimination, Geophys. J., 69, 141-161

USGS (2014). Measuring the Size of an Earthquake, U.S. Geological Survey website http://earthquake.usgs.gov/learn/topics/measure.php. Last updated February 24, 2014.

Waldhauser, F., D. Schaff, P.G. Richards, and W.-Y. Kim (2004). Lop Nor revisited: underground nuclear explosion locations, 1976-1996, from double-difference analysis of regional and teleseismic data, Bulletin of the Seismological Society of America 94: 1879-1889.

Wallace, T.C. and M.A. Tinker (1996). The Last Nuclear Weapons Test? A Brief Review of the Chinese Nuclear Weapons Program, University of Arizona http://www.iris.iris.edu/newsletter/fallnews/chinese.html

Walter, W.R., Matzel, E., Pasyanos, M.E., Harris, D.B., Gok, R., Ford, S.R. (2007). Empirical observations of earthquake-explosion discrimination using P/S ratios and implications for the sources of explosion S-waves, 29th Monitoring Research Review: Ground-based Nuclear Explosion Technologies, report of contract no. W-7405-ENG-48, 2007.

Xie, J. (2002). Source scaling of Pn and Lg spectra and their ratios from explosions in central Asia: Implications for the identification of small seismic events at regional distances, J.Geophys.Res.107,(B7),2128, doi: 10.1029/2001JB000509.

CHAPTER 2

Development of Radiative3D for Producing Synthetics

2.1 INTRODUCTION

New methods are needed to assist in the discrimination of events recorded at regional distances (NRC, 1997). Numerical methods like finite difference and finite element are prohibitively expensive for 3-D wavefield computations at high frequency (e.g., Hestholm et al., 1994). Practical calculations involving compute times of less than a day and several 10's of processors are limited to about 100 wavelengths in range. Nuclear verification requirements often need accurate wavefield predictions for 5 Hz energy at 1000 km in three dimensions. Assuming an S velocity of 3 km/sec in the crust, this would mean 2000 wavelengths in 3-D.

Sanborn (2015) developed a computer code called Radiative3D to generate synthetics in Earth models with complex deterministic and statistical structure. Radiative3D combines a radiative transport algorithm with multiple scattering, as described below.

There is still a need for validation of radiative transport calculations against 3-D numerical methods. It is known, for example, that surface wave energy is not simulated in the radiative transport method. We assume, however, that high frequency surface waves are scattered into body waves close to the source and are rarely observed beyond 100 km in the 2 to 5 Hz band. The neglect of this effect of surface to body wave scattering needs to be tested by comparing against numerical methods. This is planned in a continuation of this work by our team.

2.2 RADIATIVE TRANSPORT

Radiative transport is a physical modeling technique that tracks energy transport as a particle flux, using ray tracing to solve for the trajectories of millions of particles representing small quanta of elastic energy. It is a suitable alternative to solving the full wave equation when ray theory criteria are met, and is particularly advantageous for high frequency modeling (Margerin, 2004, Sens-Schonfelder, 2007, and Sato, 2009). Another advantage of radiative transport is that scattering from relatively small heterogeneities (on the order of a wavelength) can be handled statistically, rather than requiring ultra-fine model meshes which would otherwise be needed to simulate the heterogeneity deterministically.

The radiative transport algorithm (Shearer and Earle, 2008; Pryzbilla et al., 2009) implemented by the Radiative3D computer code discussed below permits input of relatively large 3-D models of P-velocity, S-velocity, and intrinsic attenuation, together with parameters describing relatively small statistically described structures. The source radiation pattern is specified by moment-tensor input.

2.2.1 Software Tool: Radiative3D

For a full discussion of code development, see Sanborn (2015). The code simulates realistic earthquake and explosion radiation patterns, which are parameterized via moment-tensor elements. It propagates rays in full 3D and realistically handles reflection and transmission at discontinuous interfaces, including P-wave / S-wave conversion. The code models intrinsic attenuation and scattering due to heterogeneities separately, and produces realistic scattering patterns. Possible Radiative3D outputs include synthetic envelopes, travel time curves, and videos of energy propagation through 3-D models. The code obeys energy conservation, in that the evolution of total radiated elastic energy with time is tracked. Radiative3D is well-suited to

high-frequency synthetics. Future versions of the code will include complex 3-D model structure via a tetrahedral grid structure.

2.2.2 Code Summary

Radiative3D is a computationally efficient method of synthesizing the high frequency (>2.0 Hz) seismic wave field where differences between explosion and earthquake sources are largest (Hartse et al., 1997). By incorporating both known relatively large and unknown small 3-D structures, Radiative3D can be used to predict the behavior of ratios of regional phases along specific paths, the homogenization of source radiation patterns with range, and uncertainties in travel-time picks. Radiative3D seeks to model the diffusive transport of energy through processes of multiple scattering in a medium having random fluctuations in physical properties.

Most theoretical studies of seismic scattering assume the first Born approximation, which states that only single scattering occurs and that scattering losses from the primary wave can be neglected (Frankel and Clayton, 1986). The Born approximation is valid only for weakly scattering media and appears inappropriate for many portions of the crust (Sato, 2009). Accumulation of many scatterers will distort the wavefront and produce coda in the seismograms. Following Shearer and Earle (2003),Radiative3D models multiple scattering due to heterogeneities using the following steps (see Figure 2.1):

(1) Choose a heterogeneity power spectrum for the medium (the heterogeneity power spectrum is the Fourier transform of the spatial autocorrelation of the heterogeneity).

(2) From the heterogeneity spectrum, calculate the scattering coefficient, g, which is the scattering power per unit volume.

(3) Average g for P and S waves over all angles, forming, for example, $g_o = 1/l_p$, where path l_p is the mean free path of a P wave.

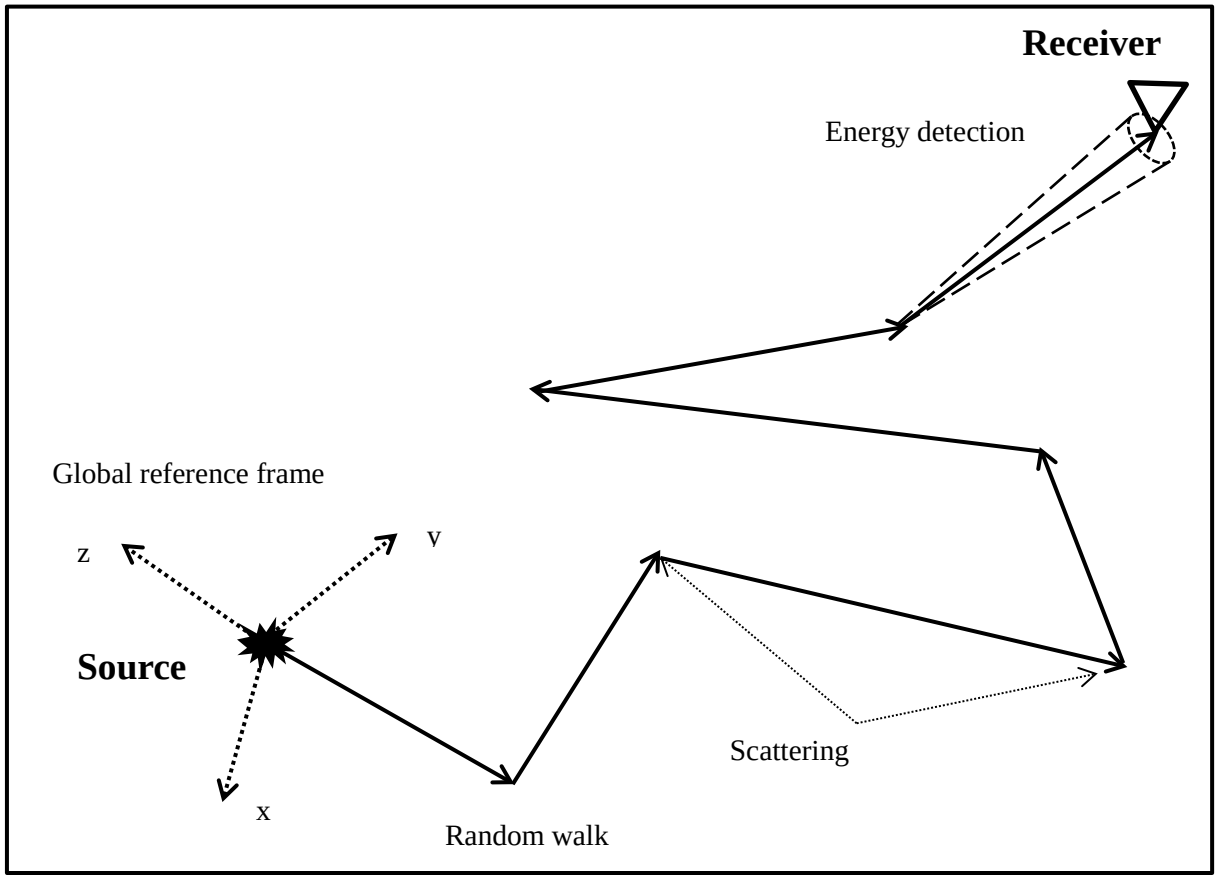

Figure 2.1. Schematic of radiative transport algorithm for coda modeling.

(4) Calculate the path length r from a discrete packet of energy emitted from a solid angle from source to a scatterer. In our work we call this packet of energy a "phonon." Assume r is an exponentially distributed random number having a mean value l_p for P waves and l_s for S waves respectively, i.e, $r_p = -\ln(x)$, where x is a random number between 0 and 1.

(5) Choose the scattered direction from sampling a probability density taken from the Born scattering coefficients of a heterogeneity model (Sato et al., 2012) and continue computing the path of the scattered energy packet. Random numbers are used to determine whether the scattering is into P or S and to determine S polarization.

Bundles of elastic energy (phonos), their amplitudes modified by multiple scattering and the source radiation pattern, are then collected at time-space bins surrounding receivers to display complete coda envelopes (Figure 2.2, left) or to display the time evolution of P and S with depth cross-sections along source-receiver paths (travel time curves, Figure 2.2, right).

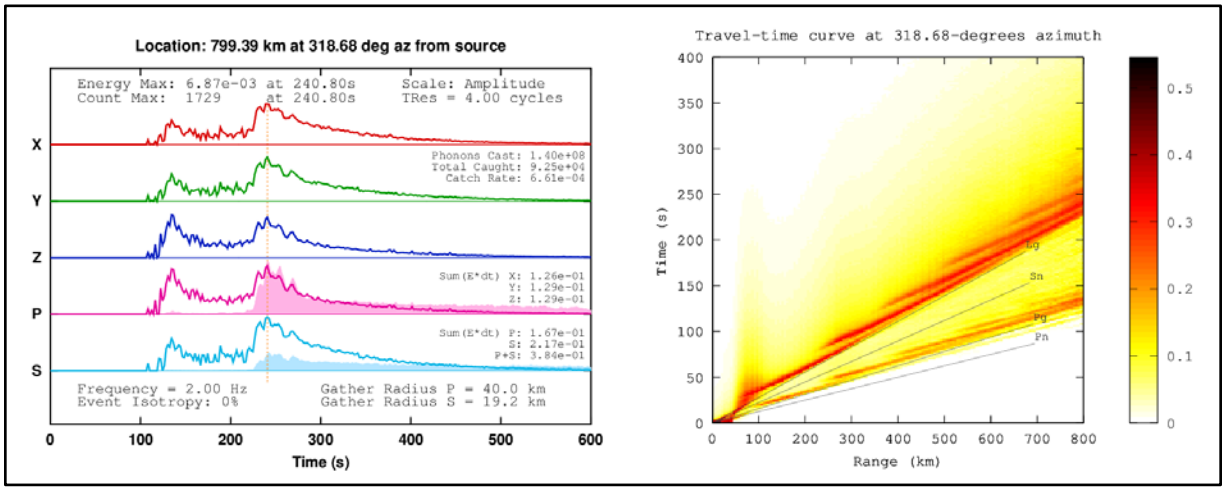

Figure 2.2. Sample Radiative3D output: coda envelope (left) and travel time curve (right).

The left figure shows narrow band (2 Hz) body wave coda synthesized for an earthquake in a 3-D model for the Lop Nor China region for a station at approximately the 800 km range. The lines are X, Y, Z, P, and S. X, Y, and Z are the directional components of motion (East-West, North-South, and Up-Down, though a future version of Radiative3D will decompose into Radial, Transverse, and Vertical). P and S are component plots in which the energy was decomposed based on arrival polarization: P or S. Note that it is based on the polarization of the phonon at the moment it hits the seismometer, *not* based on the lifetime travel history, and that there is strong conversion in the thin upper sediments layer (it's a large velocity drop), thus the Pg and Lg phases do not divide cleanly between these two traces. Future versions of Radiative3D are planned to divide up this energy based on cumulative history, which should separate the phases better.

The right side of the figure is a travel time curve showing coda envelopes for that model and earthquake source displayed as a function of distance. In the travel time curves, each pixel column represents a different envelope trace, and each column is independently normalized based on a mixture of peak-amplitude normalization and integrated-area normalization. This yields the best visual separation of phases (in our experience thus far), but does not allow for direct amplitude comparison. The travel time also includes slowness (inverse velocity) slopes for the regional seismic phases.

2.3 Earth Structure

From a modeling standpoint, we divide Earth structure into two categories, based on the approach used in the simulation (Figure 2.3):

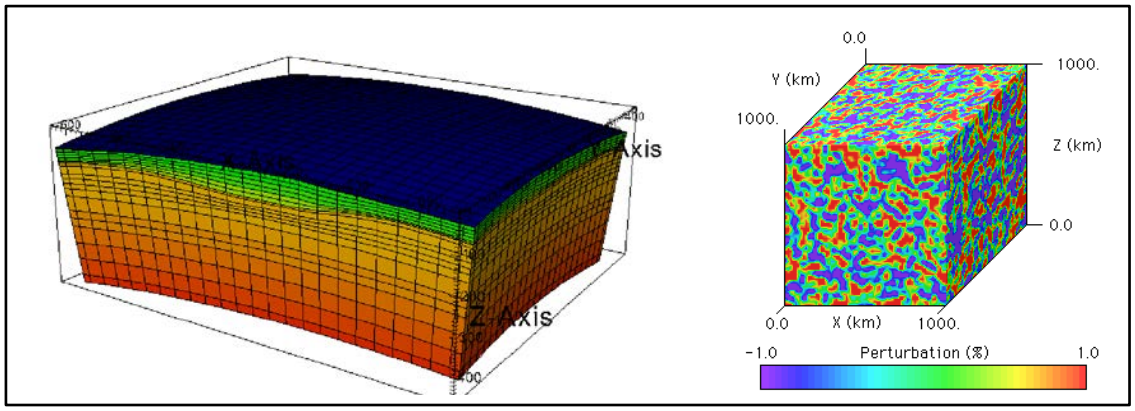

Figure 2.3. Representations of Earth structure: deterministic (left) and statistical (right).

- Deterministic structure as represented in Figure 2.3 (left), including changes in Moho depth and lateral changes in seismic velocity.
- Statistical structure, for example fine deviations of seismic velocity due to material homogeneity (represented in Figure 2.3, right), small cracks and fissures, etc.

2.3.1 Deterministic Structure

Lateral variations in crustal thickness, basin depths, mountain roots, and lateral tectonic transitions significantly affect the phases used for discrimination and detection. The Earth's large scale structures can vary with depth and are largely stratified in depth (Zheng and Wu, 2008). One example is the study by Pedersen et al. (1998), who explain anomalous Rayleigh to Love mode conversion from Lop Nor explosions by changes in crustal thickness at the boundary of the Tarim Basin and Tian Shan mountain belt. Moho topography and basin thickness can also strongly affect the propagation of Lg (Cormier and Anderson, 2004).

The scale of these types of lateral structural variations is often large enough to be resolvable by local and regional reflection and refraction experiments, gravity and magnetic data, regionalization by surficial geology, and global surface wave inversions. Hence, we refer to these types of structures as deterministic. The types of data used to infer deterministic structure are collected at widely different spatial scales (e.g., tens, hundreds, or thousands of kilometers), presenting a challenge to the parameterization of a three-dimensional model appropriate for a region surrounding a particular seismic station. The parameterization should be flexible enough to be specified at high resolution where data are available and at lower resolution where it is not. Resolution should be high to describe features important to regional wave propagation, such as Moho and basin topography, but can be lower near interfaces having smaller velocity contrasts and lower with increasing depth in the mantle, where heterogeneity power decreases.

Relatively large features (tens to thousands of kilometers) are represented in the current version of Radiative3D using a simplified Earth model serving as a stand-in for more complex models to be supported in future revisions as work on Radiative3D comes to completion.

The Earth model used in the current synthetics is a layered model consisting of layers of spatially uniform parameters (velocity, density, heterogeneity parameters, and intrinsic attenuation). The planar interfaces separating the layers need not be parallel, and in fact can take on arbitrary orientations. We have taken advantage of this freedom to construct a first-order approximation of the topography (both surface and subsurface, e.g., Moho) in the region of the Lop Nor nuclear test site. (Figure 2.4)

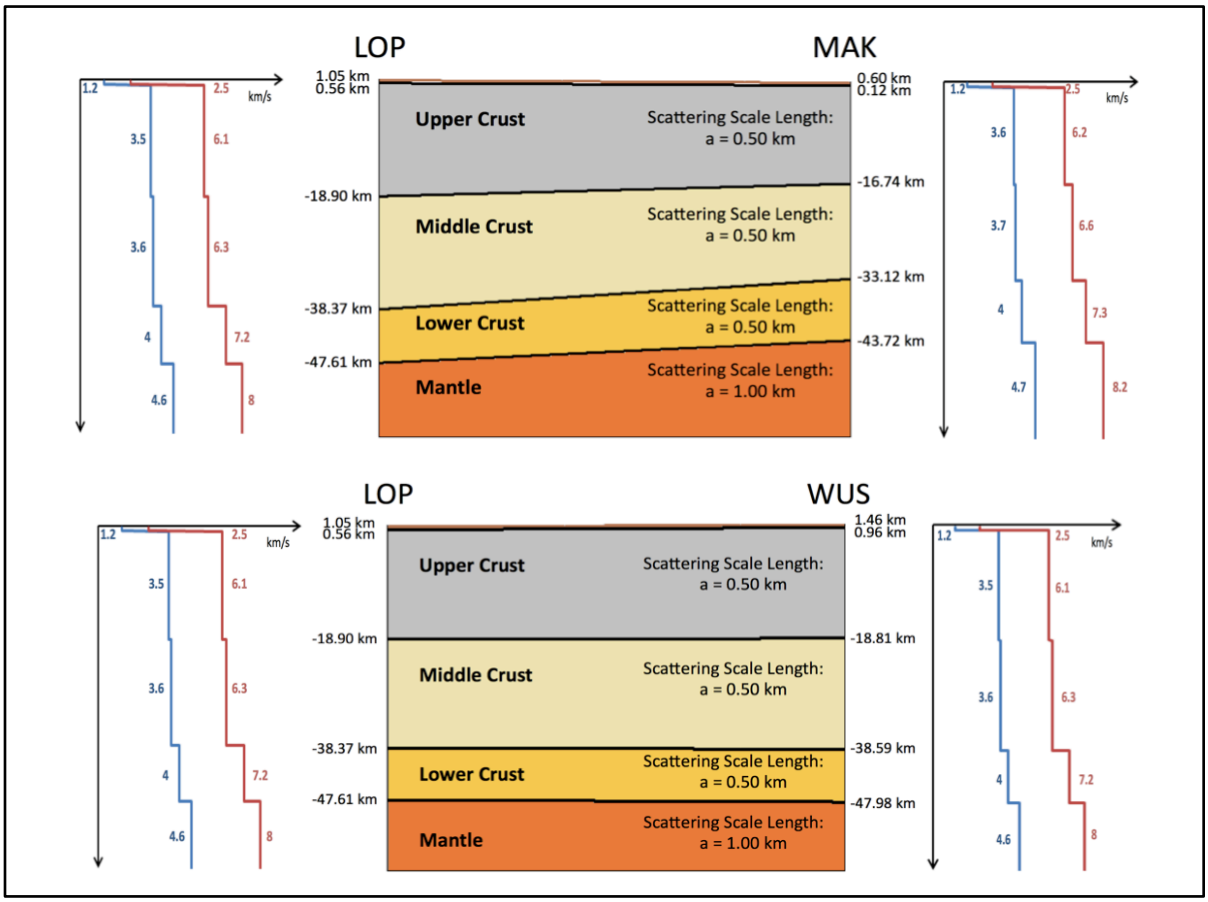

Figure 2.4. Simplified Lop Nor Earth model: Lop Nor-MAK (top) and Lop Nor-WUS (bottom).

Using known elevations of Lop Nor and seismic stations MAK and WUS, along with Moho depths from the Cornell Moho set (http://atlas.geo.cornell.edu/geoid/imagegrid.html) and layer profiles from CRUST2.0 (Laske et al., 2012) at those same locations,

we located and oriented a set of five crust layers (sediments, upper, middle, and lower crust, and top layer of the mantle). Note: CRUST 1.0 is now available (Laske et al., 2013) and will be used in future Earth models. We included information from the regionalized upper mantle (RUM) seismic model (Gudmundson and Sambridge, 1998) and defined an additional 16 mantle layers from AK-135 (Kennett et al., 1995), to a depth of 859 km. Current functionality in Radiative3D allows these interface planes to take on arbitrary orientation. Simplified model cross-sections with depth profiles between LOP and MAK and LOP and WUS are shown in Figure 2.5. These layers served as a model in which to run early test synthetics.

We later added a transition layer at the Moho to enable the synthetics to include the Moho interference seismic phases, Pn and Sn (Figure 2.5).

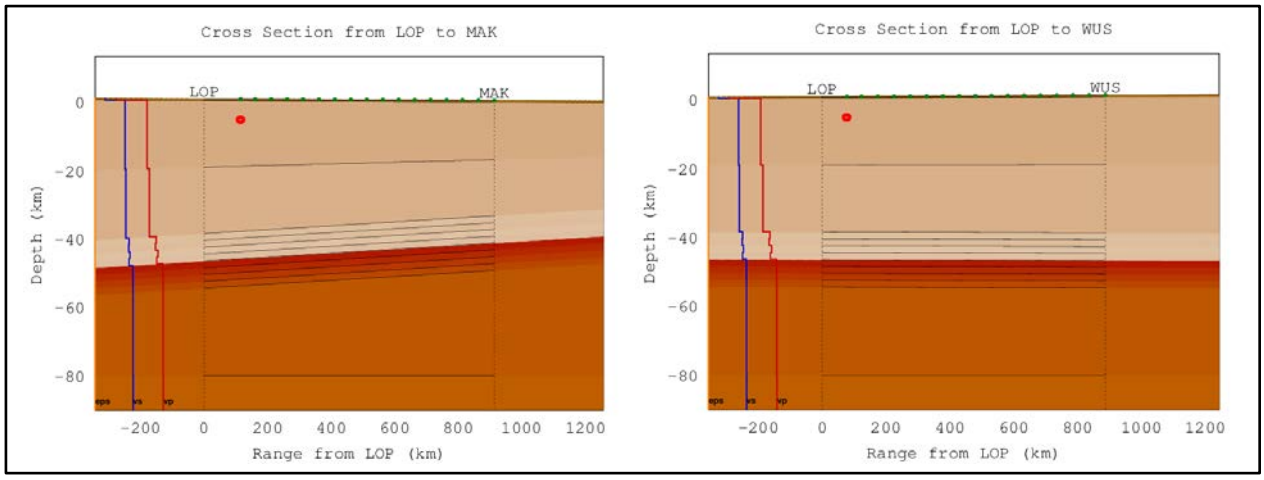

Figure 2.5. Advanced Lop Nor Earth model: Lop Nor-MAK (left) and Lop Nor-WUS (right).

The Earth model can be adjusted to include whatever layers are required for the geographic region being studied. Cao and Muirhead (1993) noted that an oceanic layer may be required to explain Lg blockage associated with oceanic paths. This could easily be accommodated in Radiative3D.

Situated within the model, we place two arrays of 160 virtual seismometers each along the paths of Lop Nor to WUS and Lop Nor to MAK (Figure 2.6). These arrays collect and bin the phonon counts to produce synthetic envelopes and travel time curves.

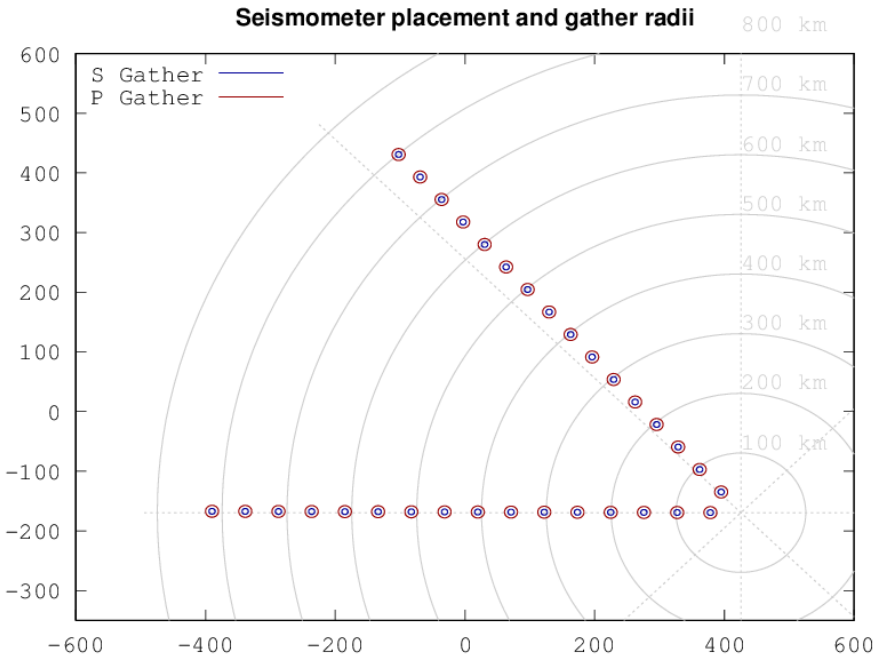

Figure 2.6. Placement of "receivers" used to produce travel time curves.

2.3.2 Statistical Structure

The amplitude of seismic waves decreases with increasing distance from the source. This attenuation is due to three effects: geometric spreading, intrinsic attenuation, and scattering (Cormier, 2011). Radiative3D addresses each of these effects.

1) Geometric spreading of seismic body waves is proportional to the reciprocal of the distance between the source and receiver.
2) Intrinsic attenuation is energy lost to heat and friction during the passage of an elastic wave and is addressed by adding a factor called Q^{-1} to the energy.

3) Scattering attenuation covers elastic energy that is not lost but scattered and redistributed into directions away from the receiver or into waves arriving in later time windows at the receiver. It is tied to random small-scale velocity perturbations throughout the crust and upper mantle represented in our work by statistical scattering.

Radiative3D also includes interface scattering tied to corrugations of the two major impedance boundaries, the free surface and the Moho.

2.3.2.1 Statistical Scattering

Scattering from relatively smaller heterogeneities (< 1 km across) represents one possible mechanism for the generation of seismic coda that is generally observed for earthquake waveforms at frequencies greater than 1 Hz. Frankel and Clayton (1986) demonstrated how earth models can be constructed that have a specified heterogeneity spectrum. The procedure consists in having perturbations at knot points driven by a random number generator, Fourier transforming the spatial model into the wavenumber domain, filtering by a desired wavenumber spectral shape, and inverse Fourier transforming back to space.

Heterogeneous media can be represented by random fields where complexities are expressed in terms of a few parameters. The auto correlation functions (ACFs) used most often by seismologists to study scattering phenomena are the Gaussian, the exponential, and the von Karman (Sato et al., 2012). Table 2.1 gives the spatial autocorrelation function (N(r)) and one- and two-dimensional Fourier transforms for these three functions (Frankel and Clayton, 1986).

The variable m is used for wave number in this table rather than the traditional k to avoid later confusion with the Von Karman coefficient κ. Figure 2.7 shows density plots of 2-D

random medium samples, where the scale length a = 5 km and the velocity perturbation ε = 0.05. The dimensions of blocks are 20 km by 20 km: (a) κ = 1.0, (b) κ = 0.5 (equivalent to exponential ACF), and (c) κ = 0.1.

Table 2.1. Correlation functions and spectra for random media.

Correlation Function	N(r)	One-dimensional Fourier Transform	Two-dimensional Fourier Transform
Gaussian	e^{-r^2/a^2}	$(\pi)^{-1/2} a e^{-m^2 a^2/4}$	$\frac{a^2}{2} e^{-m_r{}^2 a^2/4}$
Exponential	$e^{-r/a}$	$\frac{2a}{1+\mathrm{m}^2 a^2}$	$\frac{a^2}{(1+m_r{}^2 a^2)^{3/2}}$
Von Karman	$K_0\left(\frac{r}{a}\right)$	$\frac{a}{(1+\mathrm{m}^2 a^2)^{1/2}}$	$\frac{a^2}{1+\mathrm{m}_r{}^2 a^2}$

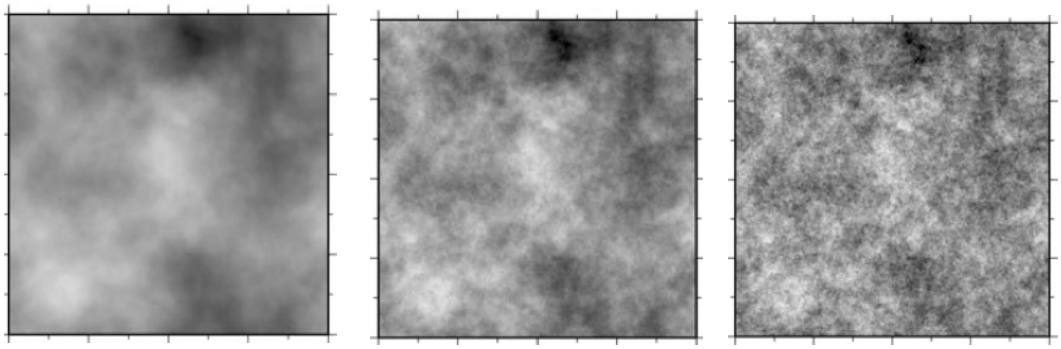

(a) κ = 1.0 (b) κ = 0.5 (exponential) (c) κ = 0.1

Figure 2.7. Density plots of 2-D random medium samples with von Karman type ACFs, where a = 5 km and ε = 0.05.
(Modified from Sato et al., 2012)

We originally chose to work with the exponential correlation, but later switched to the von Karman. This medium is "rougher" at small length scales than the Gaussian and exponential mediums and is therefore more suitable for describing lithospheric heterogeneities (Frankel and Clayton, 1986). The von Karman ACF also allows for an additional adjustment of the scattering parameters by changing the value of κ. It is also more general and flexible a description – its parameters can include the exponential autocorrelation as a special case with κ = 0.5.

A medium with the Von Karman function is characterized by heterogeneities that are self-similar for *am* > 1 (where *am* is the scale length times the wavenumber). The term "self-similar" indicates that the standard deviation of the medium, calculated over equal logarithmic intervals of wave number, remains constant over a range of length scales. Figure 2.8 shows the von Karman Power Spectral Density Function (PSDF) (P(m)) for 3-D (Sato et al., 2012). The PSDF obeys the power law for large wavenumbers.

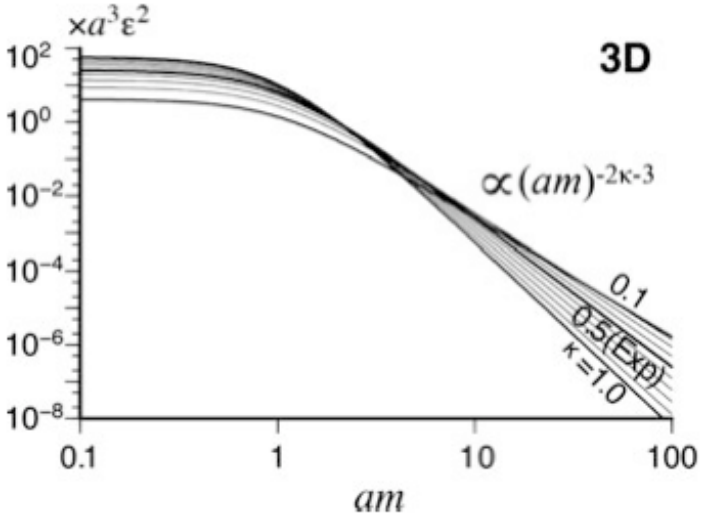

Figure 2.8. PSDF for von Karman type in 3-D.
(from Sato et al., 2012)

Sato et al. (2012 Eq. 2.13a) give the following form for the 3-D von Karman PSDF:

$$P(m) = \frac{8\pi^{\frac{3}{2}}\varepsilon^2 a^3 \Gamma(\kappa+\frac{3}{2})}{\Gamma(\kappa)(1+a^2m^2)^{\kappa+3/2}}$$

$$\approx (am)^{-2\kappa-1} \text{ for } am >> 1$$

Where: $\varepsilon = \frac{\Delta V_P}{V_P} = \frac{\Delta V_S}{V_S}$ (fractional fluctuation of the wave velocity)

a = scale length of medium (or correlation distance)

Γ is the gamma function

m is the wavenumber

κ is the von Karman order (or Hurst parameter), which varies from 0 to 1.0 as discussed above and controls the medium power spectrum roll-off with wavenumber for $am > 1$.

Radiative3D uses the *P(m)* to generate the scattering coefficients.

Sato et al. (2012) use the Born approximation for scattering due to a localized elastic inhomogeneity. They define the statistical scattering coefficients (also known as turbidity) as the scattering power per unit volume of inhomogeneous elastic media. There are four scattering coefficients:

- g^{PP} – P-to-P scattering
- g^{PS} – P-to-S scattering
- g^{SP} – S-to-P scattering
- g^{SS} – S-to-S scattering

The statistical scattering coefficients can be thought of as a 3-D probability densities for predicting scattering in various angles (see Figure 2.9). They are:

$$g^{PP}(\Psi,\xi;\omega) = \frac{l^4}{4\pi}\left|X_r{}^{PP}(\Psi,\xi)\right|^2 P\left(\frac{2l}{\gamma_0}\sin\frac{\Psi}{2}\right)$$

$$g^{PS}(\Psi,\xi;\omega) = \frac{1}{\gamma_0}\frac{l^4}{4\pi}\left|X_\psi{}^{PS}(\Psi,\xi)\right|^2 P\left(\frac{l}{\gamma_0}\sqrt{1+\gamma_0{}^2-2\gamma_0\cos\Psi}\right)$$

$$g^{SP}(\Psi,\xi;\omega) = \gamma_0\frac{l^4}{4\pi}\left|X_\psi{}^{SP}(\Psi,\xi)\right|^2 P\left(\frac{l}{\gamma_0}\sqrt{1+\gamma_0{}^2-2\gamma_0\cos\Psi}\right)$$

$$g^{SS}(\Psi,\xi;\omega) = \frac{l^4}{4\pi}\left(\left|X_\psi{}^{SS}(\Psi,\xi)\right|^2+\left|X_\xi{}^{SS}(\Psi,\xi)\right|^2\right) P\left(2l\sin\frac{\Psi}{2}\right)$$

Where:

$l = \omega/\beta_o$ is the S-wave wavenumber corresponding to angular frequency ω

$\gamma_0 \equiv \frac{\alpha_0}{\beta_0}$

Ψ and ξ are the angles from the spherical coordinate system (r,Ψ,ξ)

X is the basic scattering pattern from Figure 2.9.

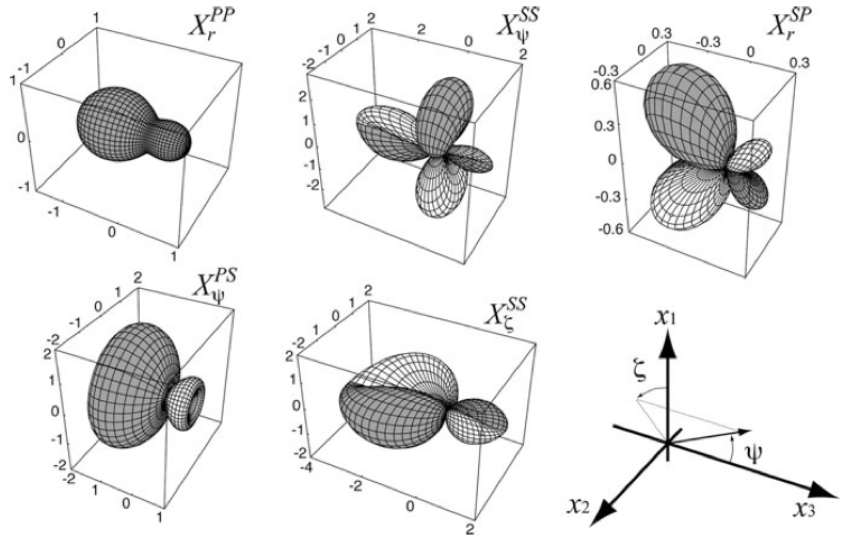

Figure 2.9. 3-D views of basic scattering patterns in 3-D elastic random media. $\gamma_0 = \sqrt{3}$, $\nu = 0.8$, and the incident wave is propagating in direction x3 and S-wave is polarized in direction x1.

(From Sato et al., 2012).

Note: $\nu = \frac{\Delta\rho/\rho}{\Delta V_P/V_P}$

According to Sato et al. (2012), the scattering contribution from the PSDF is nearly isotropic for all four scattering modes for lower angular frequencies. However, at high angular frequencies the contribution of PP- and SS-scattering is larger in a narrow cone around the forward direction compared with those at large scattering angles since the PSDF term for g^{PP} and g^{SS} is $8\pi\varepsilon^2 a^3$ for all wavenumbers at $\Psi = 0$. The product with the fourth power of wavenumber makes the scattering coefficient much larger at higher angular frequencies.

2.3.2.3 Heterogeneity Parameters Used in this Study

In Radiative3D, material heterogeneity is treated as a perturbation against locally-uniform velocity and density background. The scattering parameters used in Radiative3D are:

- ε: scattering strength, defined as the fractional velocity perturbations that characterize the heterogeneity
- ν: density perturbation – multiples ε
- *a*: characteristic scale length for heterogeneities
- κ: von Karman order number (aka, Hurst parameter)

The scale length *a* contributes to the scattering coefficients (via P(m)) and is dominant in the mean-free-path (MFP) length. The MFP can be thought of as the average distance travelled by a moving particle (or energy packet) between successive impacts (collisions or scattering incidents), which modify its direction or energy or other particle properties.

The intrinsic attenuation (quality factor Q) in included in Radiative3D ($e^{-\frac{\pi f t}{Q}}$) (Sato, 2009). It determines how many wavelengths a phonon travels before the energy is reduced by a factor of 1/e.

2.3.2.4 Interface Scattering

Radiative3D uses the reflection/transmission equations from Aki and Richards (1980) for scattering effects at the interfaces including air-sediment, sediment-crust, and crust-mantle.

2.4 Simulations of Lop Nor

We work with two types of sources in the simulations – explosions and earthquakes. Source type is input to the code using moment tensors. The moment tensor for explosions is pure P wave (isotropic) Figure 2.10 (left). For the earthquake, we use the source parameters given by Selby et al. (2005) for the March 13, 2003 Lop Nor area earthquake: strike (ϕ) = 125 ± 10^o, dip (δ) = 40 ± 10^o, and rake (λ) = 90 ± 10^o. We convert this to non-dimensional moment tensor elements using Aki and Richards (1980) to get Figure 2.10 (right). In the case of the earthquake, the standard x, y, and z axes in the tensor refer to the "North," "East," and "Down" directions.

$$\begin{vmatrix} 1 & 0 & 0 \\ 0 & 1 & 0 \\ 0 & 0 & 1 \end{vmatrix} \qquad \begin{vmatrix} -0.661 & -0.463 & -0.142 \\ -0.463 & -0.324 & -0.100 \\ -0.142 & -0.100 & 0.985 \end{vmatrix}$$

Figure 2.10. Moment tensor elements for isotropic explosion (left) and sample earthquake (right).

Bukchin et al. (2001) note that it has long been known that nearly all underground nuclear explosions have a significant component of nonisotropic seismic radiation. Patton (1991) discusses non-isotropic source effects associated with two classes of mechanisms: tectonic release and explosion-driven block motions. Bukchin et al. (2001) provide details of tectonic releases accompanying Lop Nor explosions. While we use a purely isotropic explosion source mechanism in this document, Radiative3D can easily accommodate non-isotropic components.

2.5 REFERENCES

Aki, K., and Richards, P.G. (1980). Quantitative Seismology, Theory and Methods, Vol. I and II. Freeman, New York, N.Y., 1980.

Bukchin, B.G., A.Z. Mostinsky, A.A. Egorkin A.L. Levshin, and M.H. Ritzwoller (2001). Isotropic and nonisotropic components of earthquakes and nuclear explosions on the Lop Nor test site, Pure and Applied Geophysics, 158 (2001) 1497-1515, 0033-4553/01/1497-19.

Cao, S., and K.J. Muirhead (1993). Finite difference modeling of Lg blockage, Geophys. J. Int., 115, 85-96, 1993.

Cormier, V.F., (2011). Seismic viscoleastic attenuation, in: Encylopedia of Solid Earth Geophysics, H. Gupta (ed.), pp. 1279-1290, doi: 10.1007/978-90-481-8702-7, Springer.

Cormier, V.F., and Anderson, T.S. (2004). "Efficiency of Lg propagation from SmS ray tracing in three-dimensionally varying crustal wavegudies", Pure and Appl. Geophys.,161(8), 2004, pp. 1613-1633.

Frankel, A., and R. W. Clayton (1986), Finite difference simulations of seismic scattering: Implications for the propagation of short-period seismic waves in the crust and models of crustal heterogeneity, J. Geophys. Res., 91*(*B6*)*, 6465–6489, *doi:*10.1029/JB091iB06p06465.

Gudmundson, O., and Sambridge , M. (1998). "A regionalized upper mantle (RUM) seismic model", J. Geophys. Res., 103, 1998, pp. 7121-7136.

Hestholm, S. O., Husebye, E. S. and Ruud, B. O. (1994), Seismic wave propagation in complex crust-upper mantle media using 2-D finite-difference synthetics. Geophysical Journal International, 118: 643–670. doi: 10.1111/j.1365-246X.1994.tb03991.x

Kennett, B.L.N., E.R. Engdahl, and R. Buland, (1995). "Constraints on seismic velocities in the Earth from travel times", Geophys J. Int., 122, 1995, pp.108-124

Laske, G., G. Masters, and C. Reif Z. (2012). Crust 2.0, A New Global Crustal Model at 2x2 Degrees (retrieved from http://igppweb.ucsd.edu/~gabi/crust2.html)

Laske, G., G. Masters, Z. Ma, and M. Pasyanos (2013). Update on CRUST1.0 - A 1-degree Global Model of Earth's Crust, Geophys. Res. Abstracts, 15, Abstract EGU2013-2658, 2013 (retrieved from http://igppweb.ucsd.edu/~gabi/crust1.html#reference)

Margerin, L. (2004). “Introduction to radiative transfer of seismic waves”, In: Seismic Data Analysis and Imaging With Global and Local Arrays, AGU Monogaph Series, 2004.

Patton, H. (1991). Seismic Moment estimation and scaling of the long-period explosion source spectrum, Taylor, Patton, Richards, eds., AGU Geophys. Mono. 65, 171-183.

Pedersen, H.A., Avouac, J-P., and Campillo, M. (1998). “Anomalous surface waves from Lop Nor nuclear explosions: observations and numerial modeling”, *J.Geophys. Res*., **103**, 1998, pp. 15,051-15,068.

Przybilla, J, Wegler, U., and Korn, M. (2009). “Estimation of crustal scattering parameters with elastic radiative transfer theory”, *Geophys. J. Int.*, **178**, 2009, doi:10.111/j.1365-246X.2009.04204.x.

Sanborn, C.J. (2015). *Radiative3D*: http://rainbow.phys.uconn.edu/geowiki/Radiative3D.

Sato, H. (2009). Seismic Waves in Heterogeneous Earth, Scattering of, in Encyclopedia of Complexity and Systems Science, pp. 7914-7931.

Sato, H., M.C. Fehler, and T. Maeda (2012). Seismic wave propagation and scattering in the heterogeneous earth (2nd Ed.), Springer.

Selby, N.D., D. Bowers, A. Douglas, R. Heyburn, and D. Porter (2005). Seismic discrimination in southern Xinjiang: The 13 March 2003 Lop Nor earthquake. Bulletin of the Seismological Society of America 95(1):197-211.

Sens-Schonfelder, C. (2007). Exploring Scattered Waves in Seismology

Shearer, P.M. and P.S. Earle (2004). “The global short-period wavefield modeled with a Monte Carlo seismic phonon method”, Geophys. J. Int., 158, 2004, pp. 1103-1117.

Shearer, P.M. and P.S. Earle (2008). Observing and modeling elastic scattering in the deep earth, Ch. 6, Advances in Geophysics Vol 50, Earth Heterogeneity and Scattering Effects on Seismic Wave, pp. 167-193, Sato H, Fehler M.C., Eds, San Diego, Elsevier Academic Press Inc., 2008.

Zheng, Y., and R.-S. Wu (2008). Theory of transmission fluctuations in random media with depth dependent background velocity structure, Advances in Geophysics Vol 50, Earth Heterogeneity and Scattering Effects on Seismic Waves, pp.21-41, Sato H, Fehler M.C., Eds, San Diego: Elsevier Academic Press Inc., 2008.

CHAPTER 3

Investigation of Seismic Scattering in the Crust Using Radiative3D

3.1 INTRODUCTION

Monitoring the Comprehensive Nuclear Test Ban Treaty (CTBT) requires analysts to discriminate seismic signals generated by nuclear explosions versus earthquakes or other sources of seismic energy. One of the primary obstacles to seismic discrimination or identification is an inadequate understanding of the effects of regional variations in large and small-scale crustal structure on seismic wave propagation. Analysts need a better understanding of the mechanisms that can make earthquake waveforms look similar to those from nuclear and some nonnuclear sources. Monitoring authorities need high-resolution earth models for regions of monitoring concern (NRC, 1997), and the ability to predict the effect of these models on seismic wave propagation from both earthquake and explosion sources.

For example, high frequency amplitudes seem to depend on region and path, and are related to Earth structure of various scales. Because of this effect, some events are difficult to discriminate by standard methods of high frequency amplitude ratios. It is difficult to predict these discrimination problems with current forward modeling methods. Some discriminants work better in different frequency bands. There may be some hope of regionally optimizing discriminants if structural effects can be modeled.

3.2 METHODS

New methods are needed to assist in the discrimination of events recorded at regional distances (NRC, 1997). Sanborn (2015) developed a computer code called Radiative3D to generate synthetics in Earth models with complex deterministic and statistical structure. Radiative3D combines a radiative transport algorithm with multiple scattering, as described in Chapter 2.

Radiative3D models the combined effects of known three-dimensional (3-D) deterministic Earth structure (on the order of tens to hundreds of wavelengths) and the heterogeneous statistical structure (on the order of a wavelength) to generate improved structural models. This is accomplished by synthesizing seismic envelopes using a radiative transport technique to predict the high frequency coda (>2-5 Hz) of regional seismic phases at stations having known large-scale three-dimensional structure, combined with experiments to estimate the effects of multiple-scattering.

The deterministic Earth model used in the current synthetics is a layered model consisting of layers of spatially uniform parameters (velocity, density, heterogeneity parameters, and intrinsic attenuation). The planar interfaces separating the layers need not be parallel, and in fact can take on arbitrary orientations (see Chapter 2 for more details on the Earth model). We have taken advantage of this freedom to construct a first-order approximation of the topography (both surface and subsurface, e.g., Moho) in the region of the Lop Nor nuclear test site. We chose the Lop Nor region of China as our study area for a number of reasons:

- Publicly available nuclear explosion data through the Incorporated Research Institutions for Seismology (IRIS) web site.
- Recent earthquakes near the explosion site.
- "Problem" earthquake that occurred in 2003.

The statistical heterogeneous medium is addressed in Radiative3D using the von Karman auto correlation function (ACF) with scattering coefficients from Sato et al. (2012).

For this study, we used Radiative3D to generate synthetics using two types of sources – explosions and earthquakes. The source type is input into the code using moment tensors. The moment tensor used for explosions at this time is pure P wave (isotropic). For the earthquake, we

use the source parameters given by Selby et al. (2005) for the March 13, 2003 Lop Nor area earthquake: strike (ϕ) = 125 ± 10^o, dip (δ) = 40 ± 10^o, and rake (λ) = 90 ± 10^o.

3.3 RESULTS

Radiative3D synthetic seismic envelopes are used to investigate the sensitivity of heterogeneity parameters in statistical scattering, including velocity perturbation, density perturbation, scale length, and Hurst parameter (von Karman order number). We also investigated the effects of intrinsic attenuation (Q^{-1}) and surface layer (sediments) properties, the generation of S waves by explosion sources, Moho interference phases (Pn and Sn), and differences in frequency bands.

3.3.1 Sensitivity of Heterogeneity Parameters

Radiative3D uses the scattering coefficients from Sato et al. (2012) to determine the mean free path (MFP) and scattering radiation pattern (X) for each scattering event. These coefficients were defined in Chapter 2. Each coefficient has two factors:

- The von Karman Power Spectral Density Function (P(m)) provides information about the heterogeneity characteristics and determines the MFP, which is how far the phonon travels before it encounters a scattering event.

$$P(m) = \frac{8\pi^{\frac{3}{2}}\varepsilon^2 a^3 \Gamma(\kappa + \frac{3}{2})}{\Gamma(\kappa)(1 + a^2 m^2)^{\kappa+3/2}}$$

(Sato et al. (2012, Eq. 2.13a))

Where: $\varepsilon = \frac{\Delta V_P}{V_P} = \frac{\Delta V_S}{V_S}$ (fractional fluctuation of the wave velocity)
a = scale length of medium (or correlation distance)
Γ is the gamma function
m is the wavenumber

κ is the von Karman order

- Radiative3D generates discrete packets, referred to in this work as “phonons,” emitted from a solid angle from source to a scatterer. The scattering radiation pattern (X) determines what direction the phonon takes after it is scattered, its body wave type (P or S), and its polarization of its particle motion. This aspect is captured in the calculations discussed below as a dipole projection (DP) (positive values indicate dominant forward scattering, negative indicates dominant back-scattering).

As discussed in Chapter 2, the four heterogeneity parameters that contribute to these coefficients and can be varied as input parameters are:

- Velocity perturbation or scattering strength ε (epsilon),
- Density perturbation ν (nu)
- Scale length a (in km)
- Von Karman order number (Hurst parameter) κ (kappa)

Radiative3D can be used to investigate the effects of these parameters and can be adjusted to represent regional differences. While we are able to include scattering parameters for the mantle, crust, and sediments (thin layer on top of the crust) separately, the sensitivity studies discussed in this section focus on crustal parameters.

We investigated the sensitivity of the code results to the heterogeneity parameters using two methods: (a) calculations of the mean free path (MFP) and dipole projection (DP) while varying each of the parameters and holding the others constant and (b) simulations of earthquakes and explosions at a number of frequencies and a variety of parameters. Seismic energy scattered from the heterogeneities will generally arrive in the coda following the major

seismic phases as the paths of the scattered waves (or phonons) have longer travel times than the direct arrivals (Hedlin et al. 1997).

The MFP and DP calculations provided a fairly quick and accurate way to understand the general effects of the parameters. The MFP reports how far a phonon will travel (in km) before it encounters a scattering event. Longer MFPs mean less scattering. The dipole projection gives information about the direction the phonon takes after it is scattered and varies from -1 to +1. A value of +1 means it is 100% likely to continue in its forward direction, and a value of -1 means it is 100% likely to be totally scattered backwards.

In all cases MFP is plotted on the left side *y*-axis and shown as solid lines, the DP is plotted on the right side y-axis and shown as dashed lines, and the parameter being varied is plotted on the *x*-axis. The red lines show the effect of scattering on the P-wave phonons, and the blue lines show S-wave phonons. For all parameter runs the frequency was 1 Hz, the S-wave velocity was 4.0 km/s, and the ratio of P-wave velocity to S-wave velocity (γ_0) was 1.7321.

The discussion of each heterogeneity parameter also examines the effect that parameter has on the synthetic envelopes for earthquakes and explosions compared to a baseline set of parameters (Table 3.1).

Table 3.1. Baseline heterogeneity parameters used for sensitivity synthetics.

	nu	eps	a	kappa	Q_s
Sediments	0.8	0.01	0.25	0.2	50
Crust	0.8	0.04	0.2	0.3	1000
Mantle	0.8	0.008	0.2	0.5	300

Q_P is assumed to greater than Q_S by a factor of approximately 9/4, consistent with an assumption of viscoelastic attenuation purely in shear and a Possion's ratio of 1/4 (Anderson, 1989).

The Radiative3D synthetic envelope output provides information to help analyze the effect the heterogeneity parameters have on the scattering of the seismic energy. Figure 3.1 shows the synthetic envelope for the baseline parameters listed in Table 3.1 with some of the features labeled.

- The title gives the location of the phonon capture point relative to the phonon release point in terms of distance and azimuth. This is equivalent to the seismic station location relative to the earthquake or explosion event. For the synthetics discussed in this section, the phonon release point is from the location of the 2003-03-13 earthquake and the capture point is the location of station MAK, with a gather radius of 40.0 km for the P phonons and 19.2 km for the S phonons.
- The five lines show the energy captured as a function of time. X, Y, and Z are the directional components of motion (East-West, North-South, and Up-Down), similar to those produced by most seismometer. P and S are component plots in which the energy was decomposed based on arrival polarization: P or S. Note that it is based on the polarization of the phonon at the moment it hits the seismometer, *not* based on the lifetime travel history. The P and S lines also have a shaded area representing the phonon count. The maximum phonon count and the time of its arrival is listed at the top of the figure.

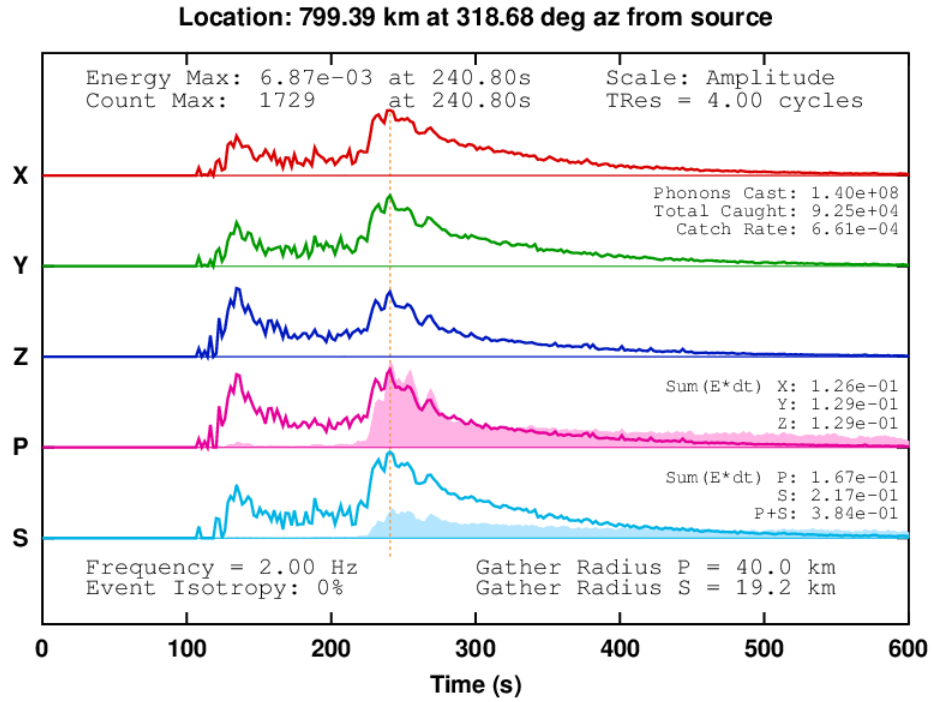

Figure 3.1. Baseline seismic envelope for earthquakes.

- The vertical dotted red line gives the location in time of the energy maximum, which is also listed at the top of the figure.
- The bottom left corner of the figure includes the frequency of the run (in this case 2 Hz) and the isotropy of the moment tensor representation of the source (0% indicates earthquakes and 100% indicates explosions).
- Phonon statistics listed on the right side of the figure include the total number of phonons cast during this simulation (in this case 140 million), the total phonons caught at this location, and the catch rate.
- Also listed on the right side is the sum of the energy captured. The total energy is indicated as P+S (3.84 e^{-01} for the baseline earthquake).

3.3.1.1 Velocity Perturbation (epsilon)

Epsilon is the fractional fluctuation of the wave velocity and is defined as $= \frac{\Delta V_P}{V_P} = \frac{\Delta V_S}{V_S}$ $\varepsilon = \frac{\Delta V_P}{V_P} = \frac{\Delta V_S}{V_S}$. Figure 3.2 shows the effects of velocity perturbations from 0.01 to 0.07 on MFP and DP. The dashed lines reflect a constant S-wave dipole projection of 0.48 and a constant P-wave dipole projection of 0.18. Varying epsilon has no effect on the scattered phonon's preferred direction of travel after scattering because epsilon is not used in the scattering pattern formula. On the other hand, there is a significant apparently exponential decrease in the MFP for both P and S phonons for this range of velocity perturbations. We should expect to see increased coda production for both S and P waves in the synthetic envelopes with increased epsilon.

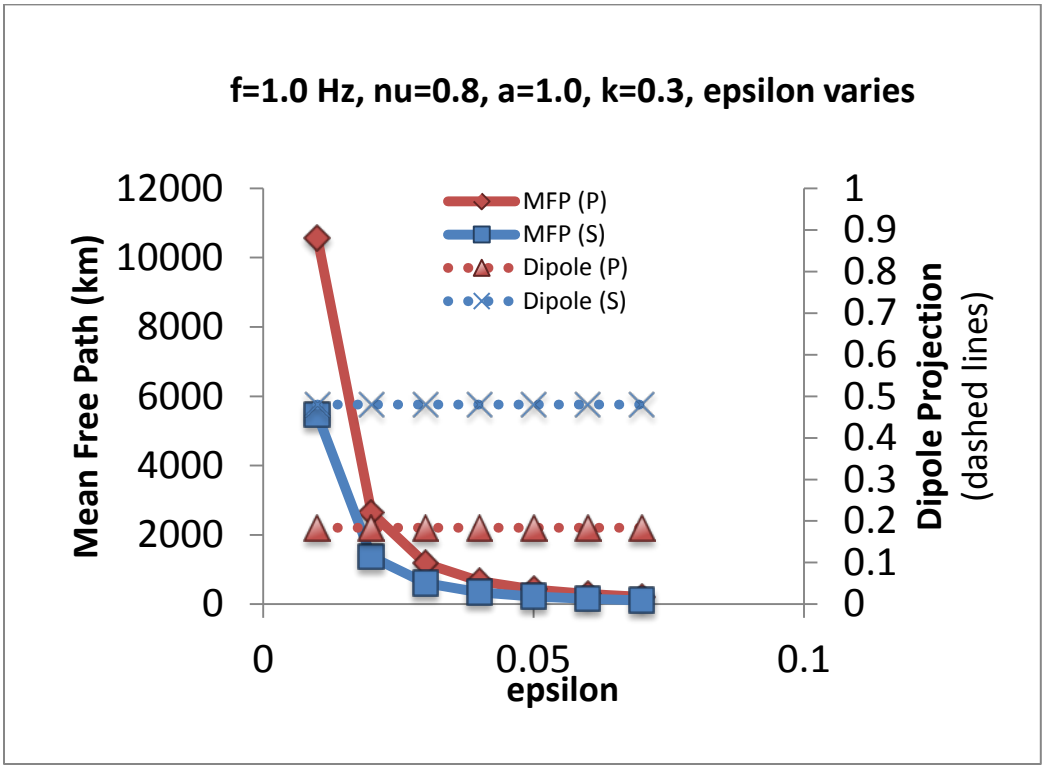

Figure 3.2. Mean free path and dipole projection for velocity perturbations.

Figure 3.3 compares a high velocity variation (epsilon) in the crust to the baseline synthetic envelopes (0.08 vs. 0.04) produced for a frequency of 2 Hz. The first peak arriving in each set of envelopes (~ 120 s) is the direct arrival of the Pg energy. The second group of energy arriving (starting at ~220 s) is the direct arrival of the Lg wave (defined as the superposition of multiple critically reflected S waves from the Moho and free surface).

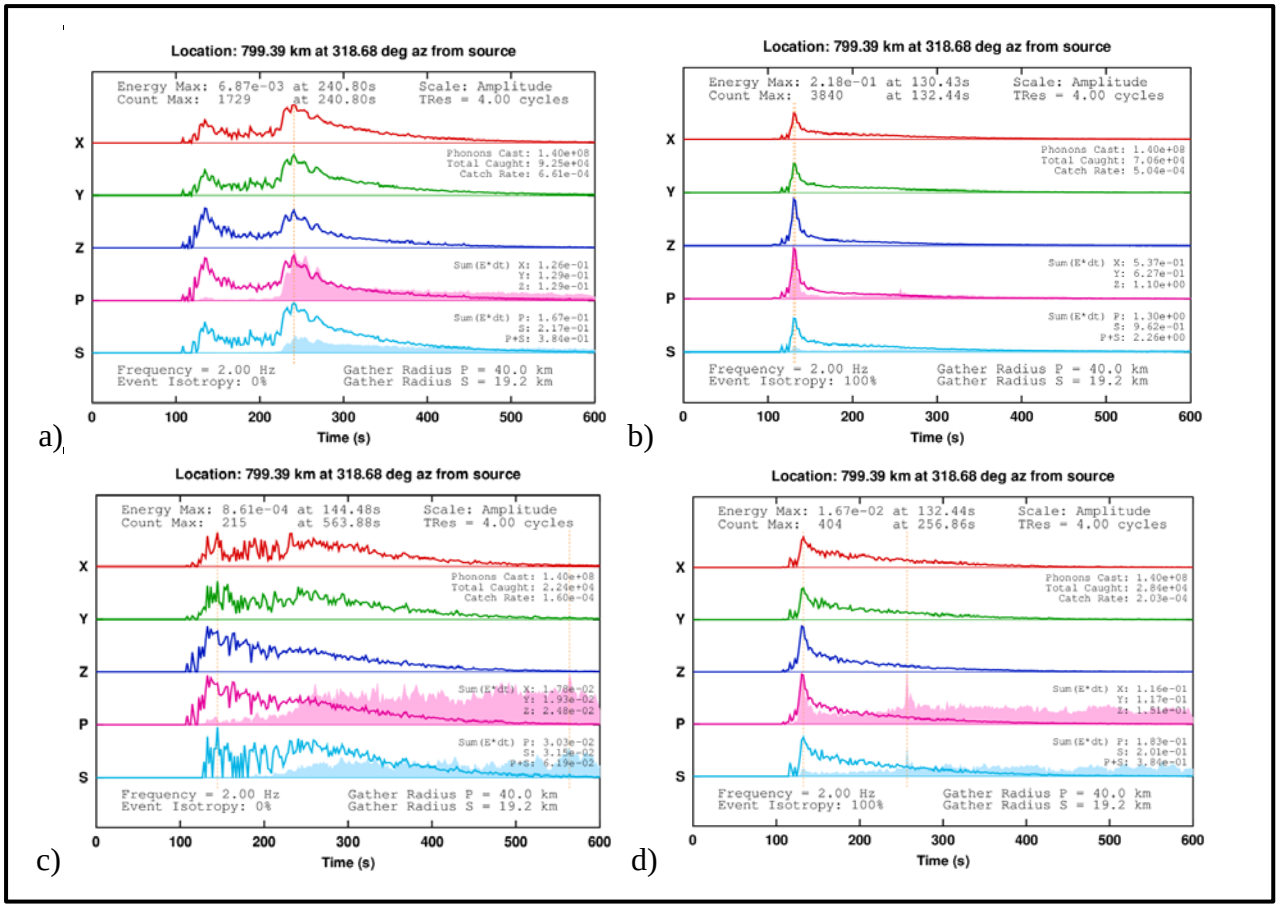

Figure 3.3. Synthetic envelopes for velocity perturbations.
a) earthquake baseline, b) explosion baseline,
c) earthquake high epsilon, d) explosion high epsilon

For the earthquake, the maximum energy and maximum phonon count in the baseline are both associated with the Lg phase (occurring at ~ 241 s). For the explosion, the maximum energy

and maximum phonon count in the baseline are both associated with the Pg phase (occurring at ~ 130 s), as would be expected.

We could see a number of effects in the seismic envelopes caused by the change in the heterogeneity parameters, including change in total energy and phonons arriving at the receiver, change in maximum energy (giving an indication of phase amplitude), onset of Pg and Lg phases, shape of direct phase arrival (pulse), and coda following the direct arrival. The earthquake with the additional velocity perturbation shows a total energy of about 16% of the baseline. The maximum energy is only 12.5% of the baseline, and it occurs at the time of the Pg arrival (~ 144 s). The total phonon energy is about 24 % of the baseline. The maximum phonon count is only 12.4% of the baseline, and it occurs much later (~ 564 s). The amplitudes on both direct arrival phases are reduced, and the peaks can barely be distinguished as separate arrivals. A majority of the energy has been delayed or diverted from the direct arrival.

The explosion with the higher velocity perturbation shows a total energy of about 17% of the baseline. The maximum energy is only 8% of the baseline, and it occurs at the same time as the baseline. The total count of phonons captured is about 40% of the baseline. The maximum phonon count is only 10.5% of the baseline, and it occurs later (~ 257 s). The onset of the Pg arrival appears to be a bit sharper. The amplitude of the Pg arrival is smaller, and the pulse is broader, with much of the energy delayed into the coda. Note that the later arriving phonons will have followed a longer total path, due primarily to multiple scattering events, so they will have less energy due geometric spreading and intrinsic attenuation losses.

The combined results of the MFP/DP and synthetic envelopes tell us that with higher velocity perturbations, the phonons have smaller mean free paths, thus encountering more scattering events. However, the lack of change in the dipole polarization tells us they tend to

scatter more towards the direction of the paths before the scattering events, so will eventually reach their original destination. The shift in arrival time of the maximum energy in the earthquake envelope from the Lg arrival window to the Pg arrival window may reflect the fact that S-waves are more sensitive to velocity fluctuations than P waves.

The scattering caused by the increase in the velocity perturbation produces a marked redistribution in energy so that it is stretched out over a longer period of time. This is represented by the lower amplitude of the solid lines, the broadening of the pulses, and a pronounced delay in the phonon arrivals (shaded area). For this sensitivity run we used an epsilon value of 0.07 (= 7%). Frankel and Clayton (1986) note that crustal velocity fluctuations could be as high as 10%, depending on the region. The results in these figures reflect the production of P and S coda energy as well as the transition from P to S energy (particularly for the explosion). Without the scattering, almost all of the explosion energy is in the Pg arrival. With the scattering, in addition to coda energy following the P-arrival, there is significant energy arriving at the time we would expect to see Lg. Unlike the higher velocity fluctuation (epsilon = 7%) found in the crust for scale lengths on the order of 1 to 10 km, Hedlin et al. (1997) find a lower perturbation exists for these scale lengths in the mantle. In the mantle, they prefer a velocity perturbation throughout the mantle of approximately 1% with a correlation length (or scale length) of 8 km.

3.3.1.2 Density Perturbation (nu)

The density perturbation is a multiplier of the velocity perturbation: $\frac{\Delta\rho}{\rho} = \nu\frac{\Delta V_P}{V_P}$. Figure 3.4 shows the effects of density perturbations from 0.3 to 1.5 on MFP and DP. Higher values of nu produce a sorter mean free path as expected, although the effect is not as pronounced as it is for

the velocity variations. The higher values of nu also lower the dipole projection, which means the phonons are scattered further away from the forward direction of travel.

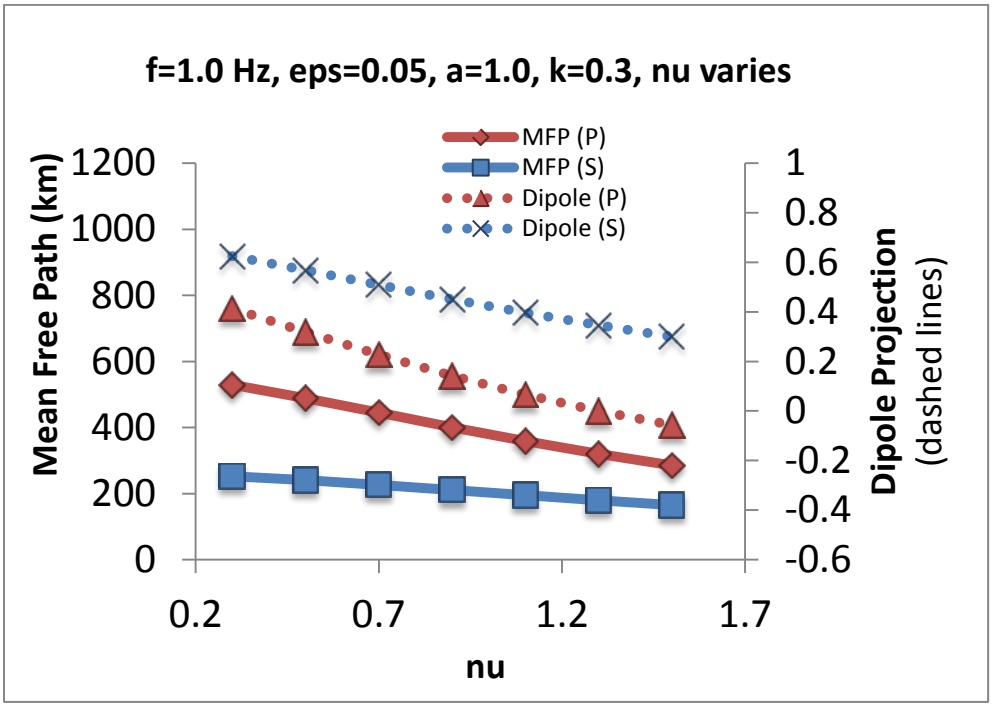

Figure 3.4. Mean free path and dipole projection for density perturbations.

Figure 3.5 compares a high density perturbation to the baseline synthetic envelopes (1.6 vs. 0.8 in the crust). For the earthquake, the increased density perturbation shows a total energy of about 57% of the baseline and a total phonon capture of 67%. The maximum energy and maximum phonon count are about 36% of the baseline. The maximum energy occurs at exactly the same time as the baseline, and the maximum phonon count occurs only slightly later (~ 255 s). The Pg onset appears to be sharper. There is a lower amplitude as some of the energy arrival is delayed, but the effect is not as pronounced as that of the velocity perturbation.

For the explosion, increased density perturbation shows a total energy of about 56% of the baseline and a total phonon capture of 87%. The maximum energy and maximum phonon count are about 43% of the baseline. They both occur at the same time as the maximum energy

arrival for the baseline. The explosion envelope has a lower amplitude but no obvious change in the Pg direct arrival pulse width or coda shape.

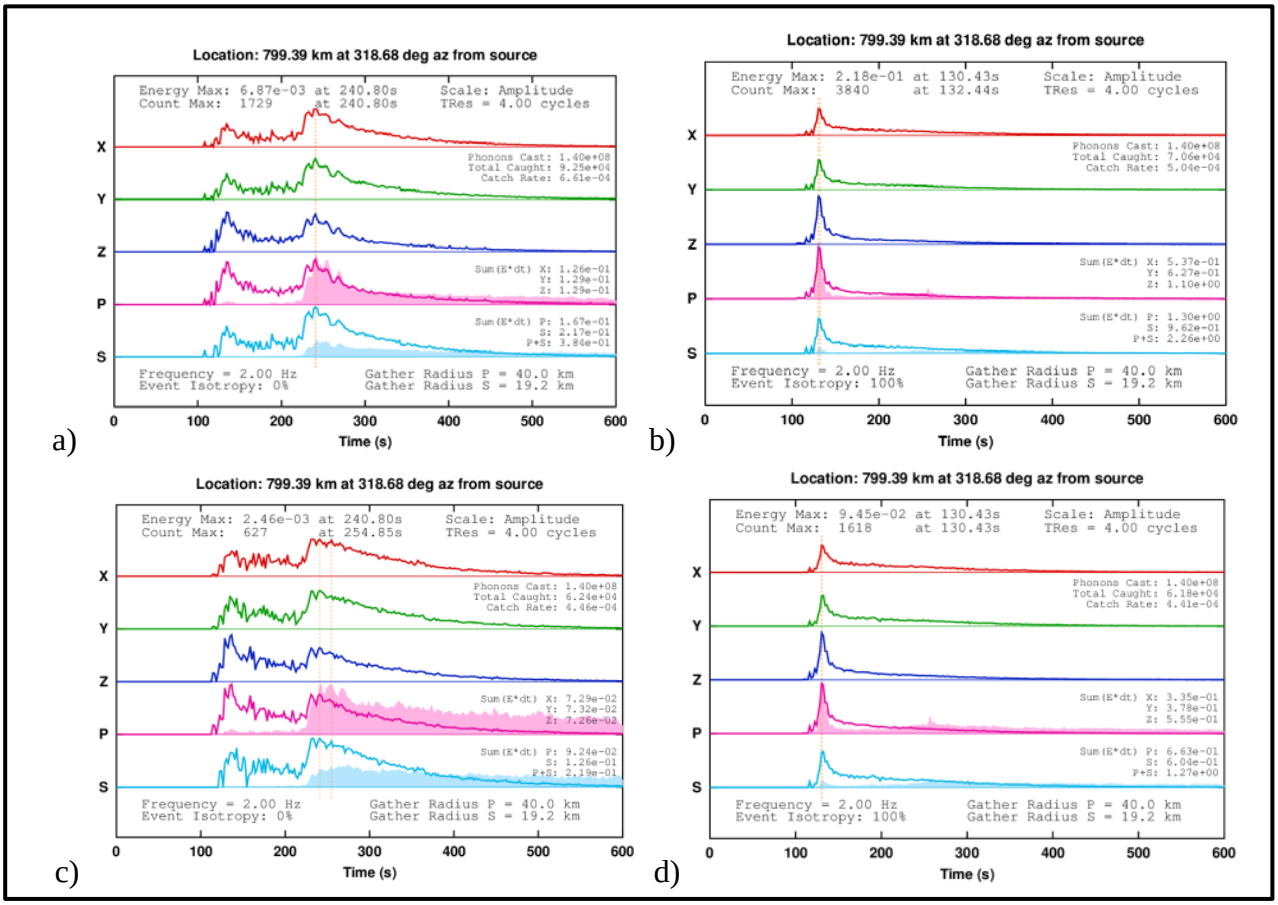

Figure 3.5. Synthetic envelopes for density perturbations.
a) earthquake baseline, b) explosion baseline,
c) earthquake high density, d) explosion high density

The combined results of the MFP/DP and synthetic envelopes tell us that with higher density perturbations, the phonons have smaller mean free paths, thus encountering more scattering events. As opposed to the effects of the velocity perturbation, they tend to be scattered further away from their original paths, so there is a reduction in energy but much less late arriving phonons than for the velocity perturbation. Since nu changes have a strong effect on the

dipole projection, they could potentially be important in estimating intrinsic Q and the separation of intrinsic Q from scattering effects. Simple Q effects are often determined from examining the decay with distance of a phase. Nu will have a different decay with distance than pure velocity fluctuations.

In general, the influence of density variations is to produce more scattered energy than for velocity variations alone. The ability to adjust *nu* could be important in other seismic coda studies, such as those involving partial melt (Hong et al., 2004). Shearer and Earle (2008) take *nu* as 0.8 for small scale heterogeneity (1-10 km). For larger structures in the mantle (hundreds to thousands of kilometers), geodynamicists take *nu* on the order of 0.2 or less because large values cannot be sustained by buoyancy (Forte et al., 1993 and Wang and Weidner, 1996). There is not really a good measure of *nu* for smaller scales other than what has been used for coda modeling in the crust.

3.3.1.3 Scale Length (a)

In the Von Karman heterogeneity spectrum, the scale length represents the corner wavenumber of the spectrum, after which the energy falls off as am (scale length times wave number) is raised to a negative power. The heterogeneity spectrum includes scale lengths above and below this value (Sato et al., 2012). Figure 3.6 shows the effects of scale length variations from 0.5 to 12 km on MFP and DP.

For the velocities and frequency used in this runs, the wavelength is 4 km for the S waves and 6.8 km for P waves. The figure shows the slope of the curves is more vertical below these scale lengths and more horizontal above these scale lengths.

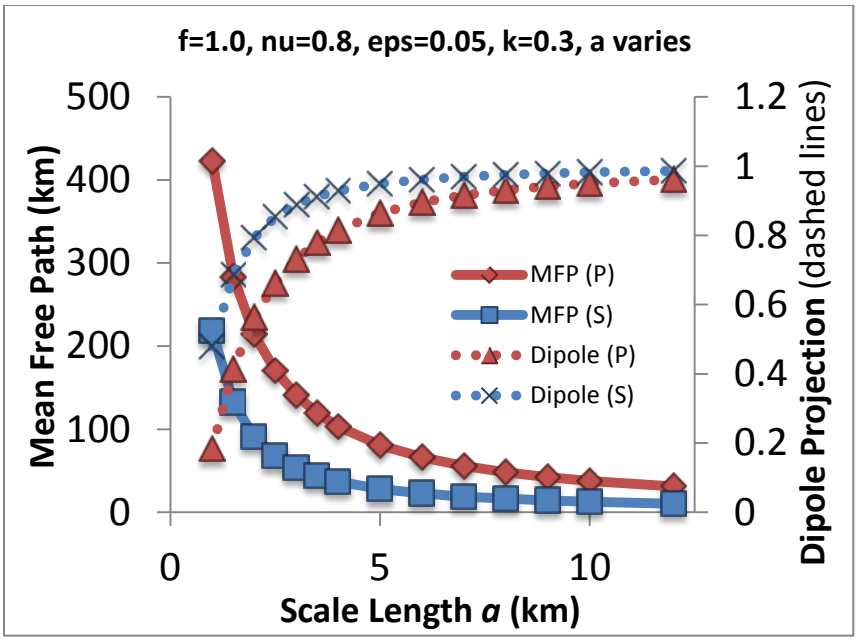

Figure 3.6. Mean free path and dipole projection for scale length variations.

Figure 3.7 shows synthetic envelopes for a three changes in the scale length: doubled compared to the baseline (0.4 km), 3 km, and 12 km. This allowed us to confirm the effects of the scale length being greater than the wavelength.

For the earthquake, the total energies arriving at the receiver compared to baseline (0.2 km) for the three values of scale length are 73% (0.4 km), 90% (3 km) and 137% (12 km). The respective maximum energies are 54%, 81%, and 160%, all arriving with a slight delay. The total and maximum phonon counts show a similar trend.

For the explosion, the total energies arriving at the receiver compared to baseline for the three values of scale length are 57% (0.4 km), 44% (3 km) and 75% (12 km). The respective maximum energies are 34%, 16%, and 46%, all arriving with a slight delay. The total phonon counts compared to baseline are 105% (0.4 km), 74% (3 km) and 78% (12 km). The respective maximum phonon counts are 36%, 20%, and 50%.

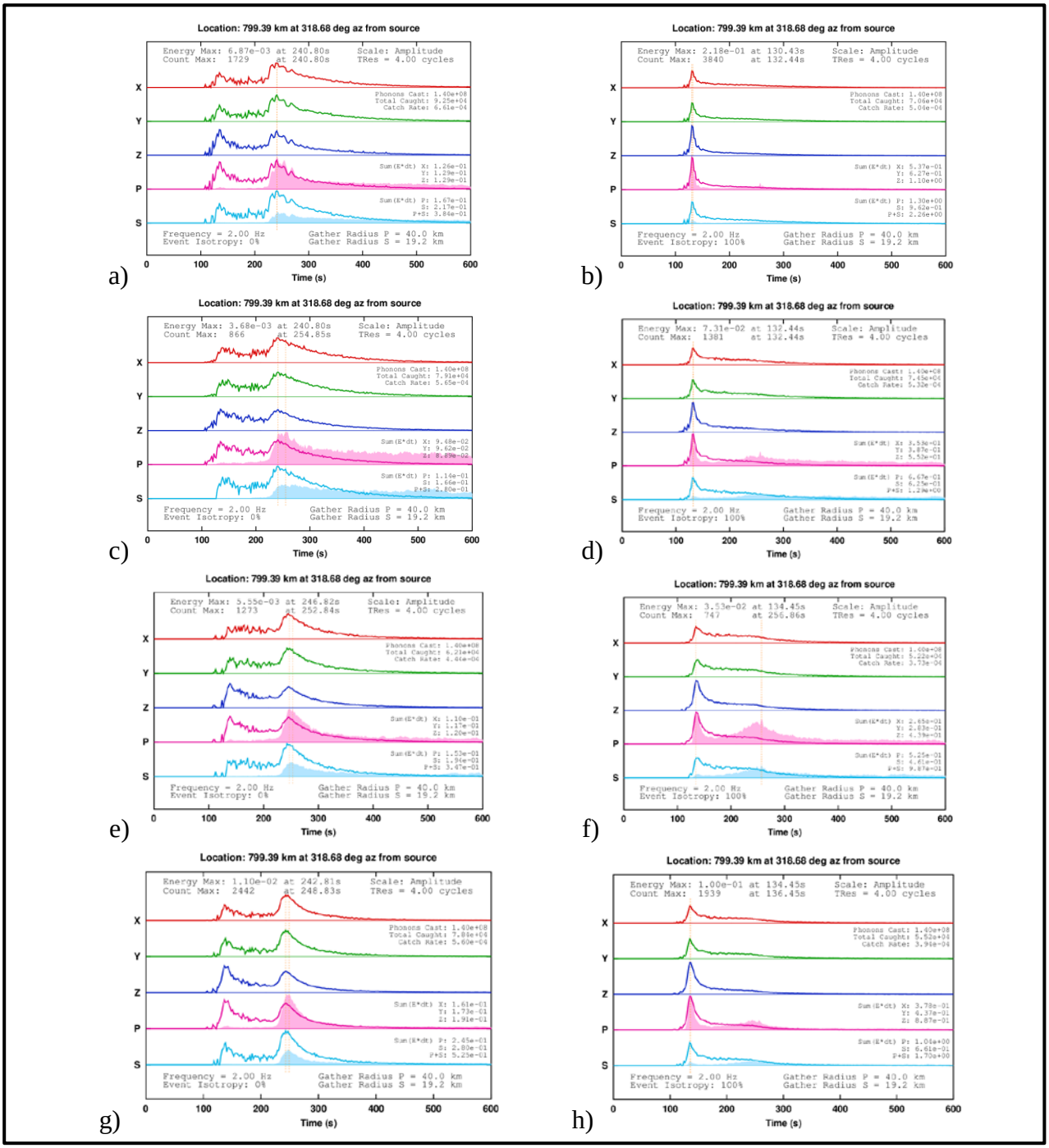

Figure 3.7. Synthetic envelopes for scale length variations.

a) earthquake baseline, b) explosion baseline,

c) earthquake 0.4 km scale length, d) explosion 0.4 km scale length,

e) earthquake 3 km scale length, f) explosion 3 km scale length,

g) earthquake 12 km scale length, h) explosion 12 km scale length

Table 3.2 summarizes the energy and phonon effects of the scale length variations for earthquake seismic envelopes and Table 3.3 does the same for explosion envelopes. In addition to the values discussed above we also looked at 2 km and 8 km. These results clearly show that the scattering due to scale length is reduced when the scale length is greater than the wavelength.

The relation between the wavelength of the seismic waves (lamda) and the size of the scatterers (a) is of critical importance in the physics of the scattering process (Aki, 1980). Frankel and Clayton (1984) note that the apparent attenuation is largest when the scatterer size is comparable to the seismic wavelength. Shorter scale lengths scatter seismic energy, broaden the waveforms of body waves, and redistribute energy into different time and angular windows (Cormier, 2011).

Table 3.2. Summary of scale length sensitivity for earthquake envelopes.

Scale length (a)	% of total energy	% of maximum energy	% of total phonon count	% of maximum phonon count
0.4 km	73	54	86	50
2 km	80	66	63	62
3 km	90	81	67	74
8 km	125	130	80	124
12 km	137	160	85	141

Table 3.3. Summary of scale length sensitivity for explosion envelopes.

Scale length (a)	% of total energy	% of maximum energy	% of total phonon count	% of maximum phonon count
0.4 km	57	34	105	36
2 km	40	15	74	19
3 km	44	16	74	19.5
8 km	65	32	77	36
12 km	75	46	78	50

3.3.1.4 Hurst Parameter (kappa)

The fluctuation spectra for the von Karman medium are flat up to a corner wave number inversely proportional to the correlation distance and then fall off at higher wave numbers (ka >

1). It is also characterized by heterogeneities that are self-similar for ka > 1. This medium is "rougher" at small length scales than the exponential medium (Frankel and Clayton, 1996).

Figure 3.8 shows the effects of *kappa* variations from 0.1 to 0.8 on MFP and DP. As kappa increases, the MFP decreases, which cause scattering delays in the energy arrival. However, as with the scale length variations, the DP shows the scattering event is more likely to be forward scattered.

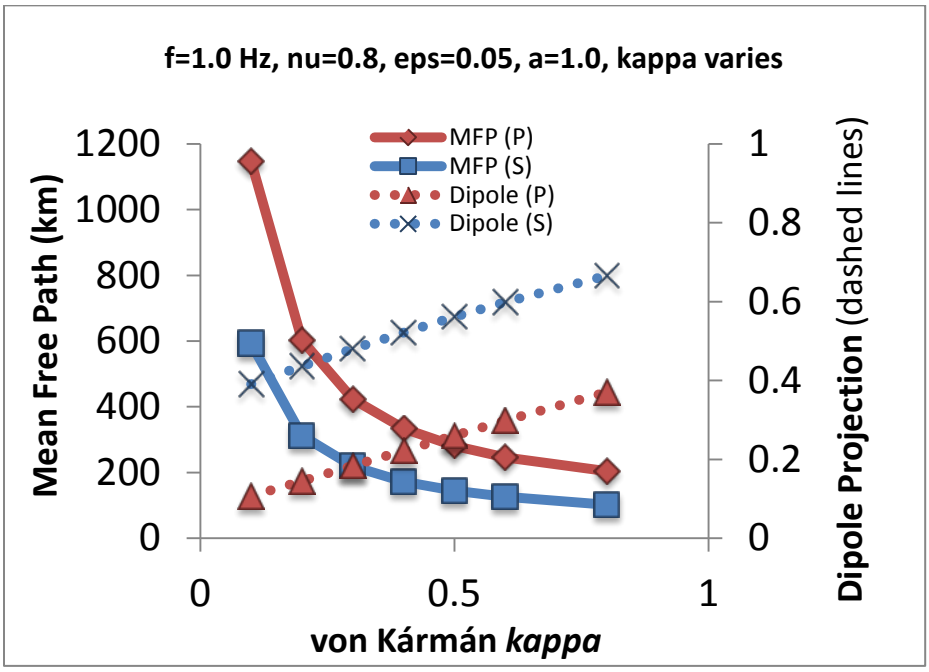

Figure 3.8. Mean free path and dipole projection for *kappa* variations.

Figure 3.9 shows synthetic envelopes with the Hurst parameter (kappa) doubled compared to the baseline. For the earthquake, the larger kappa shows a total energy of 64% of the baseline and a total phonon count of about 79% of the baseline. The maximum energy and maximum phonon count of approximately 42 % the baseline. As with the density perturbation, the maximum energy occurs at exactly the same time as the baseline, and the maximum phonon

count occurs only slightly later (~ 255 s). The effects on the direct arrival pulse widths appear to be minor.

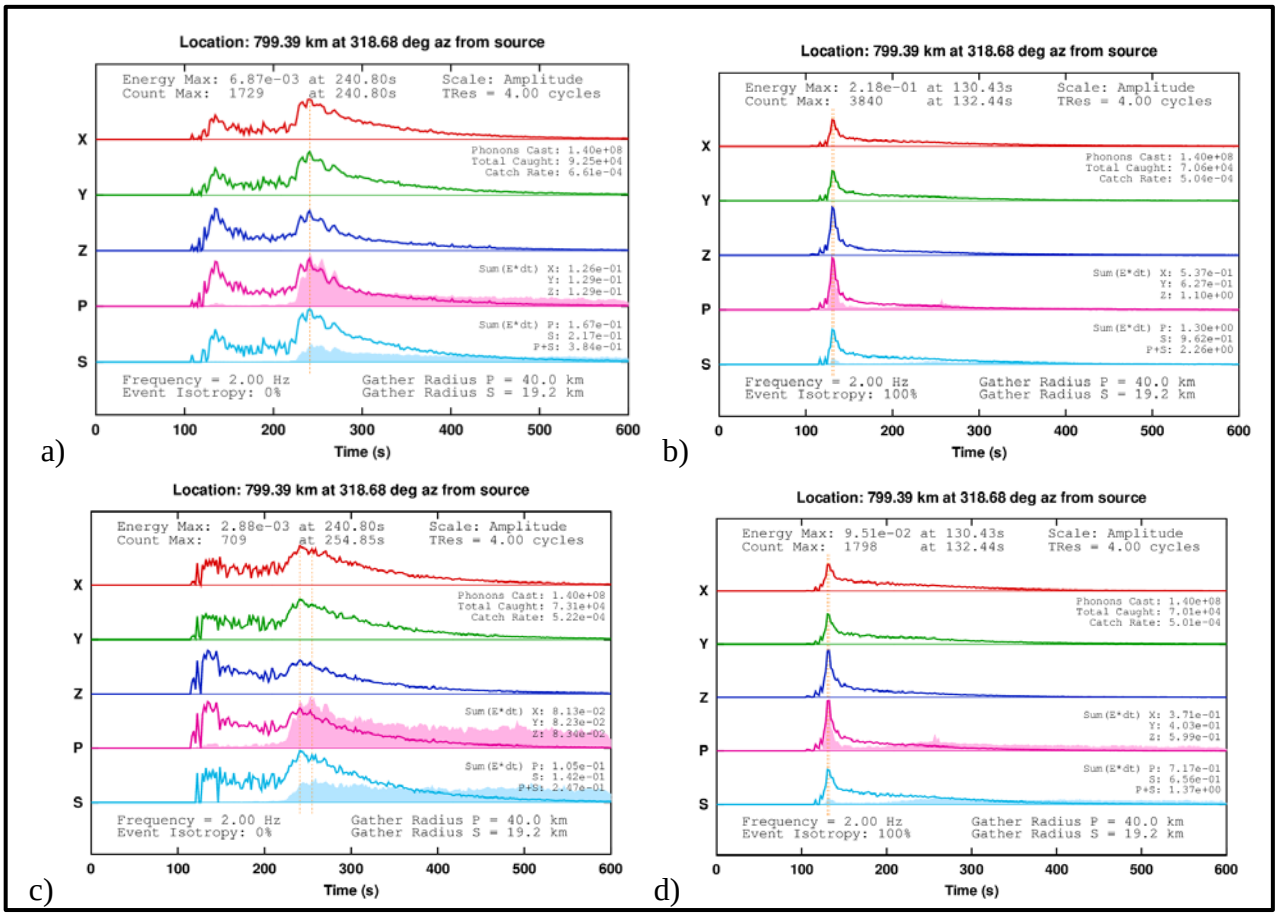

Figure 3.9. Synthetic envelopes for *kappa* variation.
a) earthquake baseline, b) explosion baseline,
c) earthquake high kappa, d) explosion high kappa)

For the explosion, the total energy is about 61% of the baseline, with a maximum energy of approximately 43.6%. The total phonon count is about 99% of the baseline with a maximum phonon count of about 47% of the baseline. As with the earthquake, the effects on the direct arrival pulse width appear to be minor.

3.3.1.5 Summary of Heterogeneity Parameter Sensitivity

Table 3.4 gives a summary of the heterogeneity parameter sensitivity for earthquakes and Table 3.5 summarizes these results for explosions. Varying each of the parameters has an effect on the scattering, and the effects are not all the same. The strongest effect in terms of amplitude reduction and delayed energy arrival is due to the change in velocity perturbation.

Table 3.4. Summary of heterogeneity parameter sensitivity for earthquake envelopes.

Parameter	Parameter change	% of total energy	% of maximum energy	% of total phonon count	% of maximum phonon count
Epsilon	2X	16	12.5	24	12.4
Nu	2X	57	36	67	36
Scale length (a)	2X	73	54	86	50
Kappa	2X	64	42	79	41

Table 3.5. Summary of heterogeneity parameter sensitivity for explosion envelopes.

Parameter	Parameter change	% of total energy	% of maximum energy	% of total phonon count	% of maximum phonon count
Epsilon	2X	17	7.7	40	10.5
Nu	2X	56	43	87	42
Scale length (a)	2X	57	34	105	36
Kappa	2X	61	44	99	47

These results show some of the potential of Radiative3D to help with our understanding of the effects of these parameters on the scattering process.

3.3.2 Intrinsic Attenuation Effects

As discussed in Chapter 2, intrinsic attenuation is energy lost to heat and friction during the passage of an elastic wave and is addressed by adding a factor called Q^{-1} to the energy. Values of Q reported in the literature often include the effects of both intrinsic attenuation and scattering. It is difficult to tell by looking at real data what the actual contributions are.

Radiative3D allows us to treat intrinsic attenuation separately from scattering to help determine their relative contributions to the total attenuation.

Figure 3.10 shows a comparison of the baseline heterogeneity parameters with and without intrinsic attenuation included. For the earthquake, the total energy without Q^{-1} included is about 100 times that of the baseline, with the maximum energy value about 50 times that of the baseline. The phonon capture is about the same. This makes sense because the effect of Q^{-1} is to reduce the amount of energy in each phonon as a function of time traveled. For the explosion, the total energy without Q^{-1} included is about 10 times that of the baseline, with the maximum energy value about twice that of the baseline. The phonon capture is about the same.

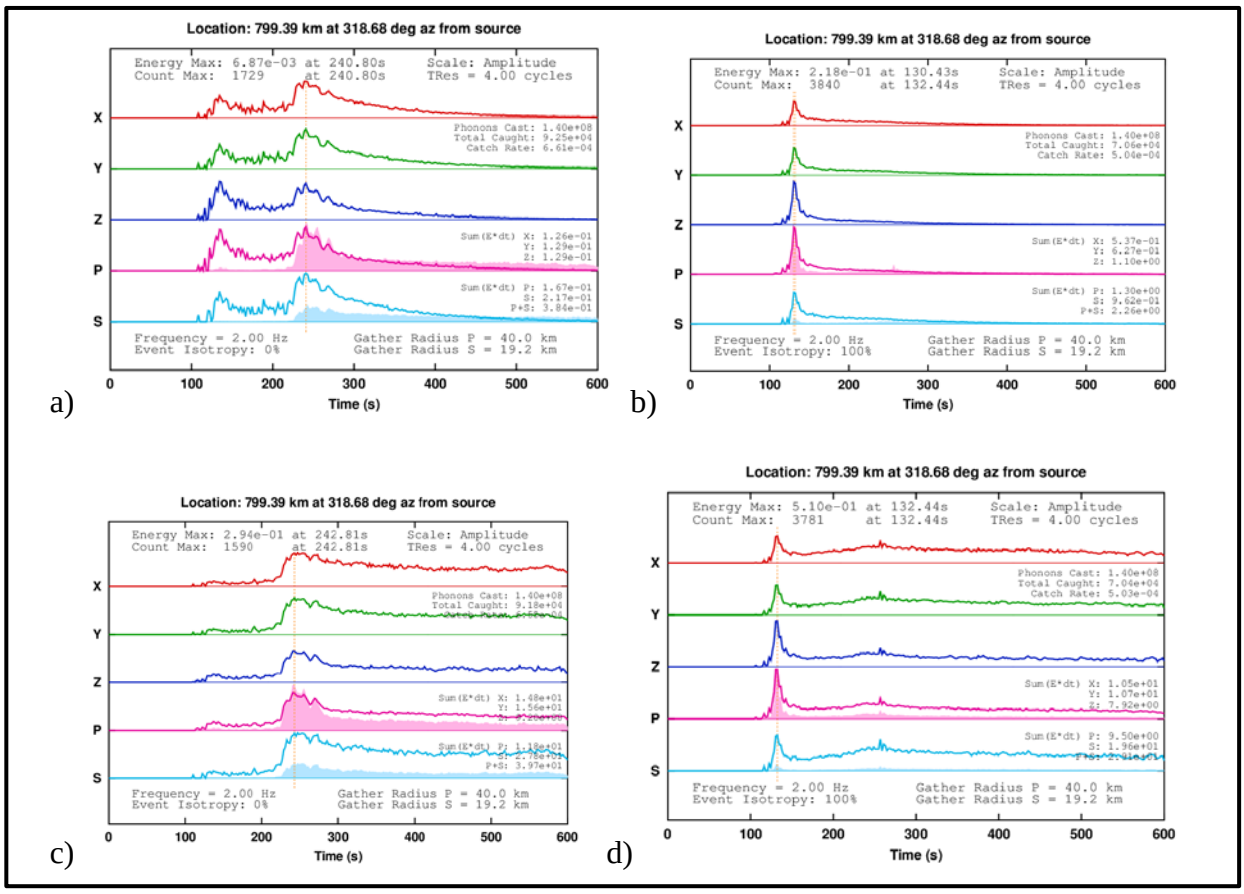

Figure 3.10. Synthetic envelopes for intrinsic attenuation effects.

a) earthquake baseline, b) explosion baseline,

c) earthquake without intrinsic attenuation, d) explosion without intrinsic attenuation

The figure shows that not adding intrinsic attenuation results in the coda energy being unrealistically high. Including Q^{-1} eliminates excess energy from the coda of the simulated and more realistically reproduces coda shape. Many, if not most experiments, have not completely removed the effects of heterogeneity on the apparent attenuation (Cormier, 2011 and Margerin, 2004). In future practice, the parameter space of scattering plus that of intrinsic attenuation can be fully explored to examine tradeoffs that can produce a fit to an object function, where the object function can be a coda envelope shape difference determined by an L-1 or L-2 norm after the phases are properly aligned. The ability to determine how much of the apparent attenuation in seismic data is due to intrinsic attenuation versus how much is due to scattering can be a very powerful tool for seismologists.

3.3.3 Surface Layer Properties

Radiative3D can be used to explore the effects of a sediments layer on the scattering envelopes. A highly heterogeneous sediment layer appears to contribute to the scattering. In the simple Earth model, the sediments layer is a thin later on top of the crust. Figure 3.11 shows example synthetic envelopes exploring the effects of the sediments layer. The envelopes in the first row (a and b) are the baselines from the heterogeneity parameter study. In the envelopes in the second row (c and d), the velocities in the sediments layer have been adjusted to nearly match those of the crust layer immediately below. This has the effect of inactivating the layer for refractive purposes. The layer is still treated separately for scattering, although for this test we set epsilon equal to 0.04, matching the values used in the crust.

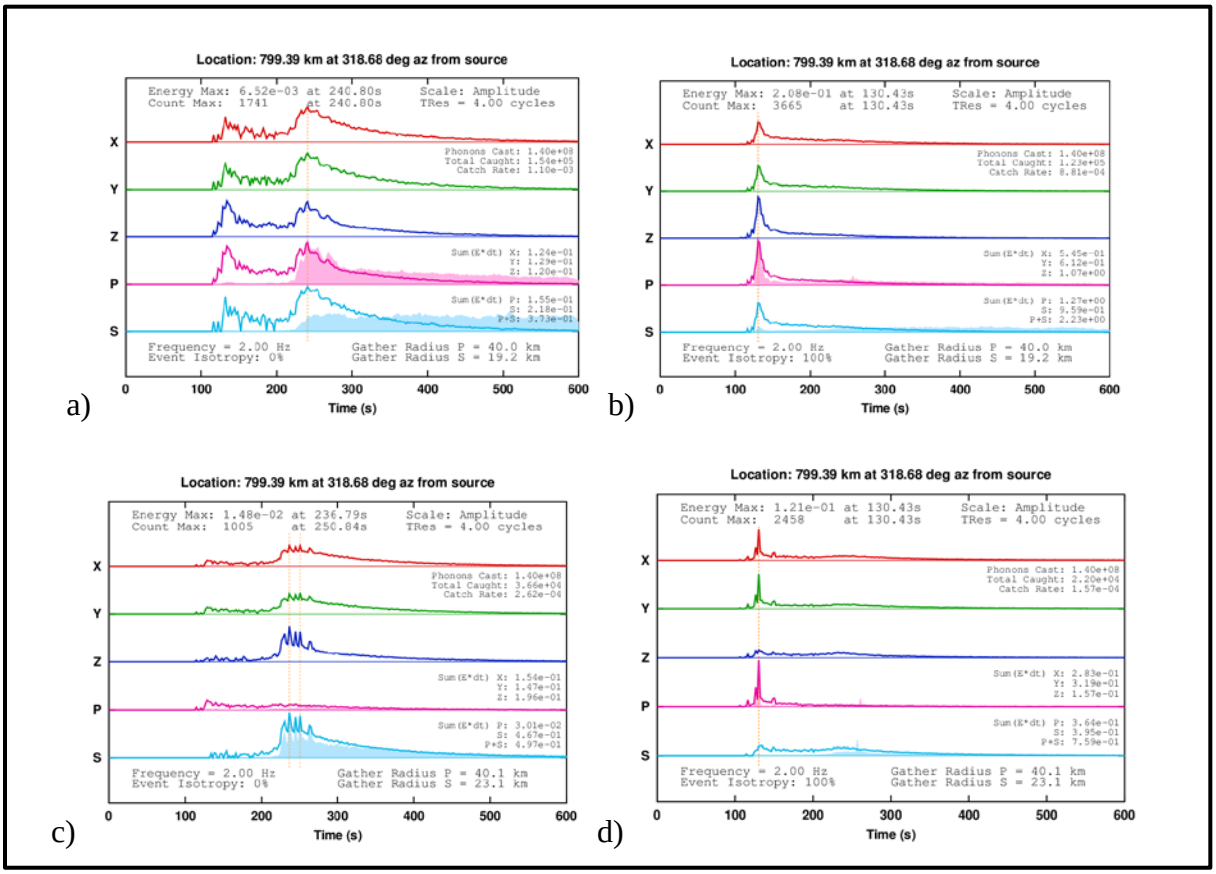

Figure 3.11. Synthetic envelopes for sediment layer effects.

a) earthquake baseline, b) explosion baseline,

c) earthquake no sediments d) explosion no sediments

The total energy without the sediments for the earthquake is 129% of the baseline, and the maximum energy is double. The total phonon count is about 40% of the baseline and the max count is 58%. This tells us that less phonons are arriving at the receiver, but they have more energy. For the explosion, the total energy without the sediments is 34% of the baseline, and the maximum energy is 31%. The total phonon count is about 56% of the baseline and the max count is 64%. The explosion receiver is getting fewer phonons and less energy.

For both the earthquake and the explosion, the most obvious result of is the effect on the phase arrival in the P and S polarization lines. For the earthquake, the Lg phase no longer shows up on the P line, and on the other lines it has so much energy that the Pg arrival can no longer be

seen. For the explosion, the Pg phase now barely shows up on the S lime. This clearly shows that the sediments later is the primary cause for the energy of what had been S phonons showing up on the P line in the results.

3.3.4 Generation of S-waves by Explosion Sources

There has been much discussion about why regional shear waves are excited by underground nuclear explosions given that the initial blast consists of only P waves (Hong and Xie, 2005, Walter et al., 2007, and references therein). One possible explanation is the contribution of multiple scattering events. Figure 3.12 shows a Radiative3D wavefront plot of phonon progression for earthquake and explosion sources as a series of time snapshops. The red dots are P-wave energy and the blue dots are S-wave energy. These plots show phonon propagation through Earth models and show how the wavefronts evolve with time. Interface reflections, ray-bending, and coda development (phonons between those concentrated along wavefronts) are all visible. Transitions between P and S polarization can happen via scattering or reflection/transmission. Transition from P to S via scattering is more probable than transition from S to P (Sato et al., 2012).

The first frame (time = 0.8 s) shows the initial P and S energy for the earthquake and the predominantly P energy for the explosion. As time progresses, we can see there is less P energy and more S energy for both the earthquake and the explosion due to predominant P to S transitions. These plots clearly show how S-waves can be produced by explosions due to multiple scattering.

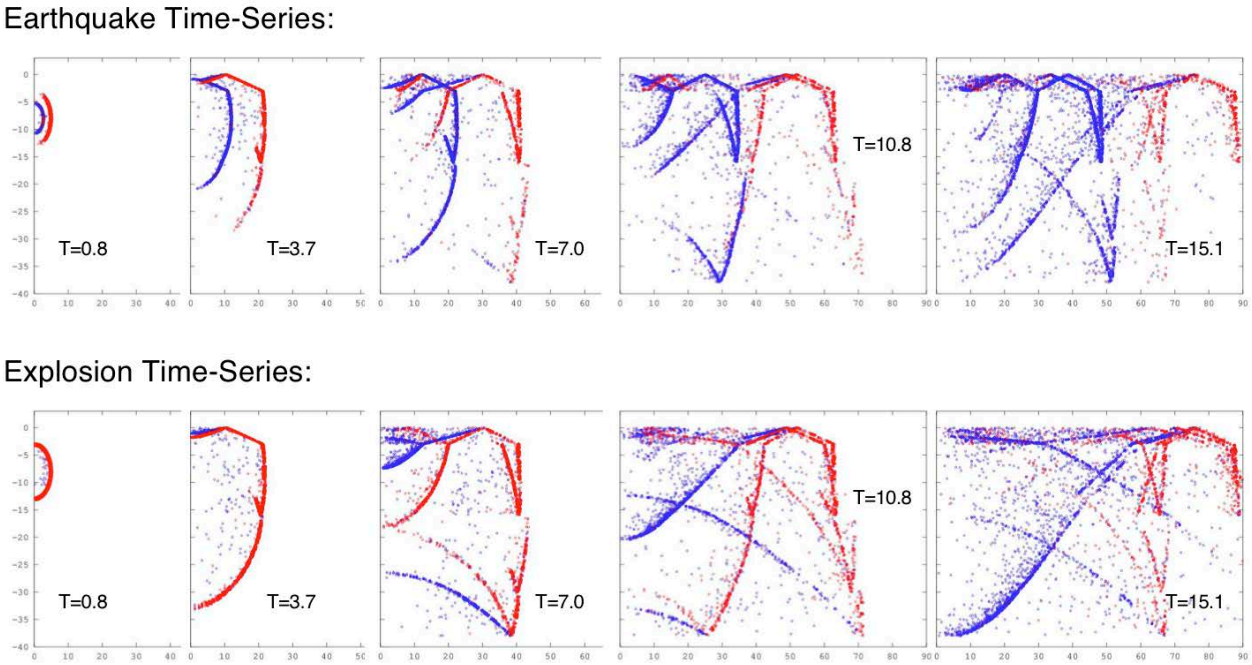

Figure 3.12. Snapshots of phonons (elastic energy bundles).

3.3.5 Moho Interference Phases

The phases Pn and Sn are not generated in the crust, and were not seen in the early synthetics generated by Radiative3D. Our group added a “transition” layer at the Moho, which includes a complex structure of velocity gradients near the base of the crust and in the mantle just below the Moho (Figure 3.13). This provides a way for rays or Pn and Sn energy to turn in the upper mantle (Cerveny and Ravindra, 1971 and Menke and Richards, 1980).

In addition, Radiative3D now includes an Earth-flattening transformation feature, which enhances ray turning potential. Figure 3.14 shows a comparison of the 2 Hz synthetics run with these features compared to data from the 2003 earthquake. The approximate arrivals from the four regional phases are marked. There is good agreement in arrival time and relative amplitude for the Pn, Pg, and Lg phases. The Sn phase is much smaller in the synthetic compared to the

data. Reducing the intrinsic attenuation may allow more of the Sn energy to show up for this phase.

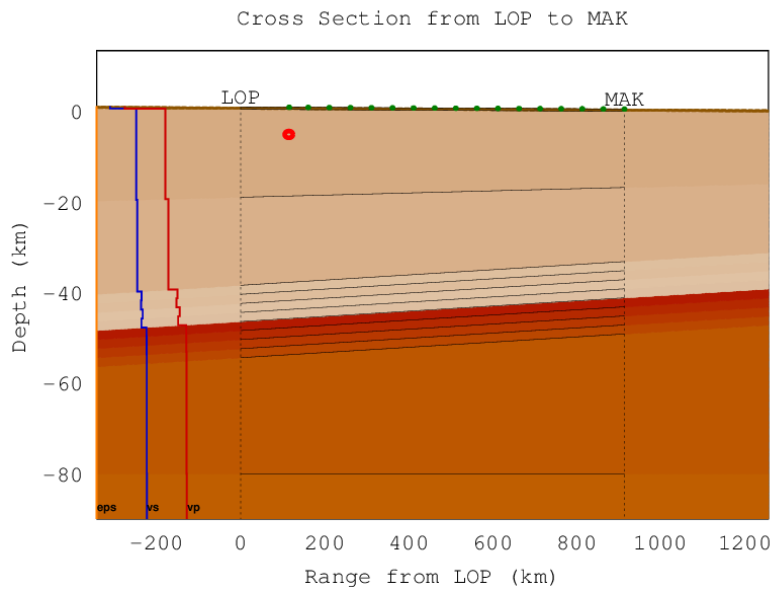

Figure 3.13. Earth model showing Moho transition layer.

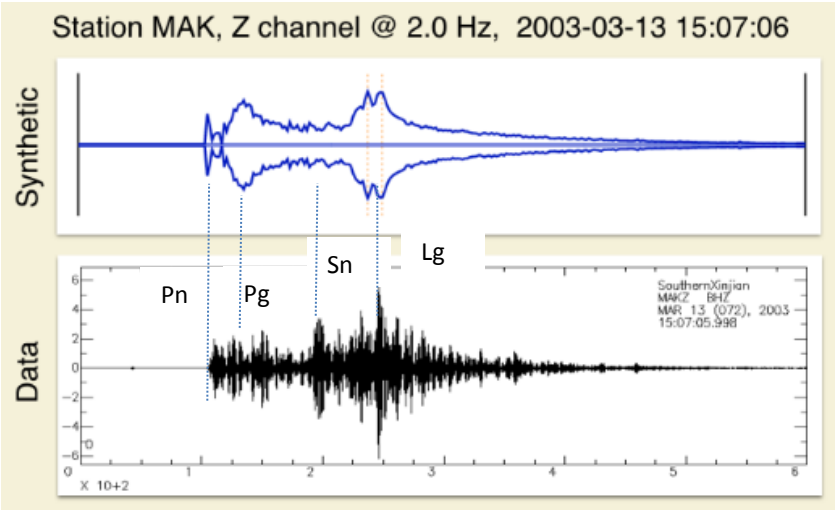

Figure 3.14. Comparison of data and synthetics including Moho transition layer.

3.3.6 Differences in Frequency Bands

Radiative3D is run at a single frequency and can create simulated seismogram envelopes at any frequency. This allows analysts to look at frequency-specifics effects on the seismic traces. Higher frequencies result in more scattering events for a given range because the mean free path between scattering events is shorter. Higher frequency runs require a greater density of solid angles to be sampled surrounding the source, and more energy packets to be tracked and summed. Earlier versions of the code required more time to run higher frequency synthetics. However, modifications in the code have made the runs faster at all frequencies.

There is now a substantial body of empirical evidence that regional P/S ratios provide poor discrimination below some frequency, typically about 2 to 3 Hz, and useful discrimination at higher frequencies (Fisk, 2006 and references therein).

Table 3.6 lists the values of the parameters used to generate synthetic envelopes that include Pn and Sn phases. These are similar to the baseline parameters used in the heterogeneity parameter sensitivity study with a transition layer added at the Moho as discussed above.

Table 3.6. Scattering parameters for frequency comparison.

	nu	eps	a	kappa	Qs
Sediments	0.8	0.01	0.25	0.2	50
Crust	0.8	0.04	0.2	0.3	1000
Transition	0.8	0.008	0.2	0.5	2000
Mantle	0.8	0.008	0.2	0.5	300

Figure 3.15 shows Radiative3D earthquake synthetics recorded at station MAK compared to actual filtered data for the 2003-03-13 earthquake for frequencies 2, 3, and 4 Hz. The approximate arrivals of the regional crustal phases (Pg and Lg) are marked. The

relative changes in amplitude of the Pg and Lg phases produced by the synthetics agree quite well with the data.

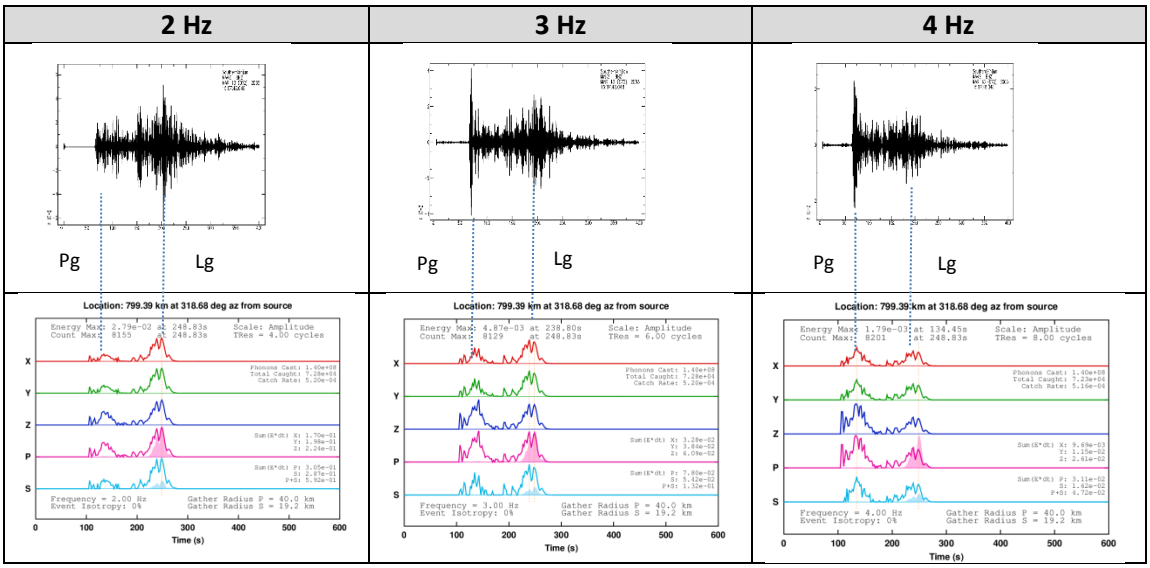

Figure 3.15. MAK earthquake data (2003-03-13) compared to synthetics at selected frequencies.

These results show us the ability of Radiative3D to produce synthetics that accurately reflect frequency effects on phase amplitude for earthquakes. Figure 3.16 shows a similar comparison for Lop Nor explosion 1996-08-06. The match of data to synthetics is not quite as good for the explosions as it is for the earthquake. Part of the reason for this is that Radiative3D uses a totally isotropic source for explosions. Seismologists have known for a long time that nearly all underground nuclear explosions have a significant component of nonisotropic seismic radiation (Bukchin et al., 2001). This can be clearly seen in the Lg energy arrival in the data. The nonisotropic component of explosions will be explored in future studies using Radiative3D. The scattering reflected in the coda of the simulated envelopes appears to roughly match that of the data. However, more work needs to be done for the synthetics to reproduce realistic envelopes.

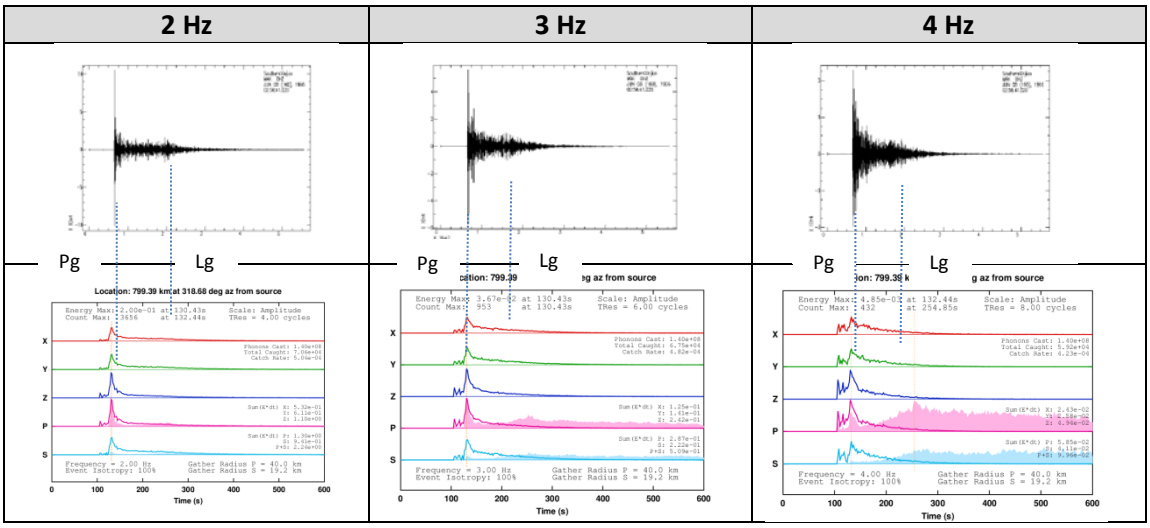

Figure 3.16. MAK explosion data (1996-06-08) compared to synthetics at selected frequencies.

3.4 SUMMARY

We have used Radiative3D to investigate the sensitivity of heterogeneity parameters in statistical scattering, including velocity perturbation, density perturbation, scale length, and Hurst parameter (von Karman order number). We also investigated the effects of intrinsic attenuation (Q^{-1}) and surface layer (sediments) properties, the generation of S waves by explosion sources, Moho interference phases (Pn and Sn), and differences in frequency bands.

Variations in each of the heterogeneity parameters influences the seismic envelopes, with velocity perturbation having the most pronounced effect. Radiative3D results confirm a number of effects discussed in the literature, including:

- The scattering effects are the strongest when the scatterer is approximately the same size as the wavelength;

- Intrinsic attenuation needs to be included in order to produce coda that match real data;
- At least some of the S-wave production by explosion sources can be explained by statistical scattering;
- The Pg/Lg ratio is affected by frequency.

In attention, we showed the contribution of the inclusion of a sediments layer to the synthetic results.

Radiative3D simulates the energy distribution at a specific frequency. It does not directly address the effect of magnitude or yield energy. The moment magnitude or yield will affect the corner frequency and therefore the contribution of the energy at the various frequencies. To see the full effect, users of the code need to "add together" the frequency contributions based on the known magnitude or yield.

3.5 FUTURE APPLICATIONS

Radiative3D has been specifically applied in this work to study the crustal effects on regional seismic waves. This technique could also be applied to other regions where small scale scattering contributions to seismic coda may be important, such as areas of partial melt, the core-mantle boundary, and the inner core/outer core boundary.

Radiative3D can be used to study any geographic region by developing coda envelopes to match the shape of real data. Users can create an Earth model based on known features produce deterministic effects (scale lengths on the order of tens or hundreds of wavelengths). The code can then be run with varying input of intrinsic attenuation and heterogeneity parameters to produce the required envelopes. Sanborn (2015) contains more information about Radiative3D.

Since this technique makes possible the modeling of 3-D effects at high frequency and longer range, which is practically inaccessible by numerical methods, it can also be potentially important for predicting earthquake strong ground motion at high frequencies (>1 Hz) and for possible earthquake locations and slip histories.

3.6 CONCLUSION

In monitoring the Comprehensive Nuclear Test Ban Treaty, one of the primary obstacles to seismic discrimination or identification is an inadequate understanding of the effects of regional variations in large and small-scale crustal structure on seismic wave propagation and understanding the mechanisms that can make seismic waveforms look similar from nuclear and some nonnuclear sources. Monitoring authorities need high-resolution earth models for regions of monitoring concern (NRC, 1997), and the ability to predict the effect of these models on seismic wave propagation from both earthquake and explosion sources.

Radiative3D is a computationally efficient method of synthesizing the high frequency (> 2.0 Hz) seismic wave field. By incorporating both known large-scale (tens of wavelengths and greater) and unknown small-scale 3-D structure (on the order of a wavelength), Radiative3D can be used to predict the behavior of ratios of regional phases along specific paths, the homogenization of source radiation patterns with range, and uncertainties in travel-time picks. Once a good model of both deterministic and statistical structure has been achieved, results demonstrate a potential for event discrimination from high frequency coda based on depth and radiation pattern.

Radiative3D helps improve the understanding of the scattering process and how it contributes to earthquake and explosion seismograms. It is a powerful method for developing

regional Earth models that take realistic Earth structure and scattering effects into account. We have made a series of parameter explorations and can conclude form these:

- Intrinsic attenuation must exist in the crust to explain coda shapes. Predicting coda shapes requires good models of both small-scale (wavelength and less) structure and intrinsic attenuation. It is possible to separate the two effects from high frequency seismic modeling of coda shapes, enabling better comparisons with laboratory work on intrinsic attenuation.
- The inclusion of a sediments layer, which can represent a thin alluvial or weathered surface layer and is characterized by more intense velocity and density fluctuations, is important for properly predicting the shapes of the coda of high frequency seismic phases used for source identification from amplitude ratios.
- S-wave production from explosions varies as a function of small-scale regional structure and path. This emphasizes the importance of gaining knowledge of this structure in regions of specific CTBT interest. For example. Hong and Xie (2005) note from the strength of mantle shear wave in the Sn window can be strongly affected by the geology of the source region.
- The amplitude ratio of the Pg and Lg phases, commonly used for event identification, is frequency dependent. This dependence includes both the statistical small-scale (wavelength and less) structure and intrinsic attenuation. Hence, its performance as a source discriminant will vary regionally, and may potentially be optimized if small-scale and intrinsic attenuation structure is known for a region.

3.7 REFERENCES

Aki, K. (1980). "Scattering and attenuation of shear waves in the lithosphere", *J. Geophys. Res*., 85, 1980, pp. 6496-6504.

Anderson, D.L. (1989) *Theory of the Earth.* Blackwell Scientific Publications, Boston, MA. ISBN 0865423350.

Bukchin, B.G., A.Z. Mostinsky, A.A. Egorkin A.L. Levshin, and M.H. Ritzwoller (2001). Isotropic and nonisotropic components of earthquakes and nuclear explosions on the Lop Nor test site, Pure and Applied Geophysics, 158 (2001) 1497-1515, 0033-4553/01/1497-19.

Cerveny, V., and R. Ravindra (1971). Theory of Seismic Head Waves, Univ. of Toronto Press, 1971.

Cormier, V.F., (2011). Seismic viscoleastic attenuation, in: Encylopedia of Solid Earth Geophysics, H. Gupta (ed.), pp. 1279-1290, doi: 10.1007/978-90-481-8702-7, Springer.

Forte, A.M., W.R. Peltier, A.M. Dziewonski, and R.L. Woodward (1993). Dynamic surface topography: a new interpretation based upon mantle flow models derived from seismic tomography, *Geophysical Research Letters*, Vol. 20, No. 3, pp. 225-228. February 5, 1993.

Frankel, A., and R. W. Clayton (1984), A finite-difference simulation of wave propagation in two-dimensional random media, *Bulletin of the Seismological Society of America*, Vol. 74, No. 6, pp. 2167-2186, December 1984.

Frankel, A., and R. W. Clayton (1986), Finite difference simulations of seismic scattering: Implications for the propagation of short-period seismic waves in the crust and models of crustal heterogeneity, J. Geophys. Res., 91*(*B6*)*, 6465–6489, *doi:*10.1029/JB091iB06p06465.

Hedlin, M.A.H., P.M. Shearer, and P.S. Earle (1997). Seismic evidence for small-scale heterogeneity throughout the Earth's mantle, Nature, Vol 387, 8 May 1997, pp. 145-150.

Hestholm, S. O., Husebye, E. S. and Ruud, B. O. (1994), Seismic wave propagation in complex crust-upper mantle media using 2-D finite-difference synthetics. Geophysical Journal International, 118: 643–670. doi: 10.1111/j.1365-246X.1994.tb03991.x

Hong, T.-K., B. L. N. Kennett, and R.-S. Wu (2004*)*, Effects of the density perturbation in scattering, *Geophys. Res. Lett.*, 31, L13602, doi:10.1029/2004GL019933.

Hong, T.-K., and J. Xie (2005), Phase composition of regional seismic waves from underground nuclear explosions, *J. Geophys. Res*., 110, B12302, doi:10.1029/2005JB003753.

Margerin, L. (2004). “Introduction to radiative transfer of seismic waves”, In: Seismic Data Analysis and Imaging with Global and Local Arrays, AGU Monogaph Series, 2004.

Menke, W. H. and P. G. Richards (1980), Crust-mantle whispering gallery phases: A deterministic model of teleseismic Pn wave propagation, J. Geophys. Res., 85*(*B10*)*, 5416–5422, *doi:*10.1029/JB085iB10p05416.

NRC (1997). National Research Council Panel on Basic Research Requirements in Support of Comprehensive Test Ban Monitoring. Research Required to Support Comprehensive Nuclear Test Ban Treaty Monitoring. National Academy Press, ISBN: 0-309-59079-5, 150 pages, (1997), http://www.nap.edu/catalog/5875.html

Sanborn, C.J. (2015). *Radiative3D*: http://rainbow.phys.uconn.edu/geowiki/Radiative3D.

Sato, H. (2009). Seismic Waves in Heterogeneous Earth, Scattering of, in Encyclopedia of Complexity and Systems Science, pp. 7914-7931.

Sato, H., M.C. Fehler, and T. Maeda (2012). Seismic wave propagation and scattering in the heterogeneous earth (2nd Ed.), Springer.

Shearer, P.M. and P.S. Earle (2008). Observing and modeling elastic scattering in the deep earth, Ch. 6, Advances in Geophysics Vol 50, Earth Heterogeneity and Scattering Effects on Seismic Wave, pp. 167-193, Sato H, Fehler M.C., Eds, San Diego, Elsevier Academic Press Inc., 2008.

Walter, W.R., Matzel, E., Pasyanos, M.E., Harris, D.B., Gok, R., Ford, S.R. (2007). Empirical observations of earthquake-explosion discrimination using P/S ratios and implications for the sources of explosion S-waves, 29th Monitoring Research Review: Ground-based Nuclear Explosion Technologies, report of contract no. W-7405-ENG-48, 2007.

Wu, R.S. and K. Aki (1988). Multiple scattering and energy transfer of seismic waves - separation of scattering effect from intrinsic attenuation II. Application of the theory to Hindu Kush Region, PAGEOPH., Vol. 128, Nos. 1/2, 1988, pp. 49-80.

Wang, Y. and D.J. Weidner (1996). $(\partial\mu/\partial T)_P$ of the lower mantle, PAGEOPH, Vol. 146, Nos. 3/4, 1996.